# AOI 1 — COMPUTATIONAL ENERGY SCIENCES: MULTIPHASE FLOW RESEARCH

# High-fidelity multi-phase radiation module for modern coal combustion systems

Final Scientific/Technical Report
Reporting Period: 08/15/2010 – 11/14/2013
Michael F. Modest, Shaffer and George Professor of Engineering
DOE Award Number DE-FE0003801
School of Engineering, University of California, Merced
Merced, CA 95343

#### Disclaimer

This report was prepared as an account of work sponsored by an agency of the United States Government. Neither the United States Government nor any agency thereof, nor any of their employees, makes any warranty, express or implied, or assumes any legal liability or responsibility for the accuracy, completeness, or usefulness of any information, apparatus, product, or process disclosed, or represents that its use would not infringe privately owned rights. Reference herein to any specific commercial product, process, or service by trade name, trademark, manufacturer, or otherwise does not necessarily constitute or imply its endorsement, recommendation, or favoring by the United States Government or any agency thereof. The views and opinions of authors expressed herein do not necessarily state or reflect those of the United States Government or any agency thereof.

#### **Abstract**

The effects of radiation in particle-laden flows were the object of the present research. The presence of particles increases optical thickness substantially, making the use of the "optically thin" approximation in most cases a very poor assumption. However, since radiation fluxes peak at intermediate optical thicknesses, overall radiative effects may not necessarily be stronger than in gas combustion. Also, the spectral behavior of particle radiation properties is much more benign, making spectral models simpler (and making the assumption of a gray radiator halfway acceptable, at least for fluidized beds when gas radiation is not large). On the other hand, particles scatter radiation, making the radiative transfer equation (RTE) much more difficult to solve. The research carried out in this project encompassed three general areas: (i) assessment of relevant radiation properties of particle clouds encountered in fluidized bed and pulverized coal combustors, (ii) development of proper spectral models for gas-particulate mixtures for various types of two-phase combustion flows, and (iii) development of a Radiative Transfer Equation (RTE) solution module for such applications. The resulting models were validated against artificial cases since open literature experimental data were not available. The final models are in modular form tailored toward maximum portability, and were incorporated into two research codes: (i) the open-source CFD code OpenFOAM, which we have extensively used in our previous work, and (ii) the open-source multi-phase flow code MFIX, which is maintained by NETL.

#### **Contents**

**References Cited** 

| 1 | EXECUTIVE SUMMARY |   |    |  |
|---|-------------------|---|----|--|
| 2 | REPO              | RT DETAILS  | 2  |  |
|   | 2.1               | Radiation Models in Fluidized Bed and Pulverized Coal Combustors        | 2  |  |
|   | 2.2               | Spectral Radiation Properties of Gas Mixtures with Common Coals         | ć  |  |
|   | 2.3               | Spectral Module for Radiation in Multi-Phase Mixtures                   | 5  |  |
|   | 2.4               | Photon Monte Carlo with Energy Splitting Across Phases for Gas–Particle |    |  |
|   |                   | Mixtures  | 18 |  |
|   | 2.5               | Test and Validation Runs  | 28 |  |
| 3 | Summ              | nary  | 39 |  |
|   |                   |   |    |  |

39

#### 1 EXECUTIVE SUMMARY

Thermal radiation, chemical kinetics, and turbulence individually are among the most challenging fundamental and practical problems of computational science and engineering. In fossil fuel processes using coal, such as coal gasifiers, reactors used for post- and pre-combustion CO<sub>2</sub> capture, and emerging technologies such as oxyfuel combustion, multiphase flow adds to the challenge. Little attention has been paid to date to accurate modeling of radiative heat transfer in any combustion systems, in spite of the fact that radiation is often the dominant mode of heat transfer (being ignored or treated with simplistic "optically thin" and "gray" models); this is true for gaseous fuel combustion [1,2], as well as for coal combustion with its strong particle radiation. In chemically reacting turbulent flows, radiation, kinetics, and turbulence are coupled in interesting and highly nonlinear ways, leading to interactions between turbulence and chemical kinetics (turbulence–chemistry interactions: TCI) and between turbulence and thermal radiation (turbulence–chemistry interactions: TRI). Both have profound influences on flame behavior but, while turbulence–chemistry interactions have received a great deal of attention over the years [3,4], the TRI have essentially been ignored, even though TRI can be just as or even more important than TCI [5–9].

It is well-established today that neglecting radiation in atmospheric pressure gaseous combustion systems may lead to *overprediction* of temperature of up to 200 °C, while using the usually-employed optically-thin or gray radiation models lead to *underprediction* of up to 100 °C and more [10,11]. Probability density function (PDF) based calculations of the PI have shown that TRI always increases the heat loss from a flame, and that this additional heat loss can reach 60% of the total and more, leading to a reduction in the local gas temperature of 200 °C or more. Therefore, in many turbulent flames accurate prediction of radiation and TRI can be at least as important as accurate modeling of combustion rates and turbulence–chemistry interaction. This is expected to be even more true for the upcoming noncrude-oil-based fuels obtained from coal through Fischer–Tropsch processes, fuels obtained from biomass, and oxyfuel processes designed for CO<sub>2</sub> capture, because these have a higher content of radiating species in their products, resulting in strong increases in optical thickness.

The effects of radiation in particle-laden flows have not yet been accurately quantified and were the object of the present research. The presence of particles increases optical thickness substantially, making the use of the "optically thin" approximation in most cases a very poor assumption. However, since radiation fluxes peak at intermediate optical thicknesses, overall radiative effects may not necessarily be stronger than in gas combustion. Also, the spectral behavior of particle radiation properties is much more benign, making spectral models simpler (and making the assumption of a gray radiator halfway acceptable, at least for fluidized beds when gas radiation is not large). On the other hand, particles scatter radiation, making the radiative transfer equation (RTE) much more difficult to solve.

The research carried out in this project extended our work to include radiation from radiating large particles, and encompassed three general areas: (i) assessment of relevant radiation properties of particle clouds encountered in fluidized bed and pulverized coal combustors, (ii) development of proper spectral models for gas—particulate mixtures for various types of two-phase combustion flows, and (iii) development of a Radiative Transfer Equation (RTE) solution module for such applications. The resulting models were validated against artificial cases since open literature experimental data were not available. The final models are in modular form tailored toward maximum portability, and were incorporated into two research codes: (i) the open-source CFD code OpenFOAM, which we have extensively used in our previous work, and (ii) the open-source multi-phase flow code MFIX, which is maintained by NETL.

- (1) Spectral radiation properties of particle clouds The particles encountered in fluidized bed and pulverized coal combustors may consist of coal, ash, lime stone, etc., with widely varying size distributions and particle loading. To make efficient and accurate calculations necessary, the particle properties were classified, pre-evaluated and stored in appropriate databases.
- **(2) Spectral radiation models for particle clouds** The high-fidelity spectral radiation models that we have developed for atmospheric pressure combustion were extended to the large absorbing/emitting–scattering particles present in fluidized bed and pulverized coal combustors. In particular, this required new gas–particle mixing models and consideration of scattering (in spectral models and in the RTE solver).
- (3) RTE solution module Two RTE solver modules were generated as appropriate for fluidized bed and pulverized coal combustors. This includes a  $P_1$  solver (for the mostly prevalent optically thicker applications) with a regression (for particles) and k-distribution (for gases) spectral module, and a photon Monte Carlo solver (for validation and for optically thinner applications) fitted with a line-by-line accurate spectral module.
- **(4) Validation of radiation models** The property databases and radiation models was validated to the extent possible by comparison with experimental data available in the literature. Simulations were carried out for fluidized beds and pulverized-coal flames, but adequate parameters and data could only be gleaned from a couple pulverized-coal flame papers.

# 2 REPORT DETAILS

#### 2.1 Radiation Models in Fluidized Bed and Pulverized Coal Combustors

As indicated earlier the state-of-the-art of radiation modeling in fluidized bed combustors and pulverized coal combustors was extremely poor, and what little work that had been done appears to have been carried out in Europe and East Asia. Paper after paper, e.g. [12, 13], reiterates that radiative transfer dominates heat transfer rates in both fluidized bed and pulverized coal combustors, yet radiation was, at worst, commonly neglected, or, at best, treated using primitive models, such as the Stefan–Boltzmann  $T^4$ -power-law.

Several competing solution methods have been developed for the five-dimensional RTE, such as the zonal method, spherical harmonics method, discrete transfer method, discrete ordinates method, and the statistical Monte Carlo method (given in roughly historical sequence) [14]. Today, because of its ease of implementation, the discrete ordinates method (DOM) and its modern cousin, the finite volume method (FVM), are perhaps the most popular, and are implemented in some form in virtually all commercial CFD solvers. However, because of large computational cost, generally only fairly low-order FVM calculations are carried out, which suffer greatly from ray effects: accurate FVM simulations require a directional grid as fine as the spatial one. Pulverized coal flames and fluidized beds tend to be optically thick and, therefore, the  $P_1$  method is the ideal RTE solver for such applications. The Monte Carlo method, while computationally expensive, can readily be implemented for even the most difficult radiation problems (strong spectral, spatial and directional variation of radiation properties, etc.) and, as such, also enjoys a certain, rapidly increasing popularity. The stochastic nature of PDF schemes makes them ideal candidates for the use of a photon Monte Carlo RTE solver.

Previous work of the PI was carried out with a number of different CFD codes (ACFlux, Fluent, OpenFOAM), which are finite-volume codes for gases, and contain Lagrangian transport equations for droplets and particles, but no detailed multi-phase interaction models. For the present project MFIX (Multiphase Flow with Interphase eXchanges), which is a general-purpose computer code developed at the National Energy Technology Laboratory (NETL) for describing the

hydrodynamics, heat transfer and chemical reactions in fluid-solids systems, in particular fluidized bed and pulverized coal combustors was installed at our UCMerced computer cluster, and was used along with OpenFOAM for radiation module development. A radiative property database of common coal particles was developed (to be used with, both, conventional and statistical RTE solvers), a  $P_1$  RTE solver was implemented in MFIX, an accurate spectral module for conventional solvers (such as  $P_1$ ) was developed, and (mostly for validation purposes) also a multi-phase LBL-accurate stochastic Monte Carlo RTE solver was implemented in MFIX and OpenFOAM.

# Spectral Radiation Properties of Gas Mixtures with Common Coals

To calculate the full-spectrum k-distribution of a gas-particle mixture, we use databased narrowband k-distributions [15] of the combustion gases and mix them based on the Modest-Riazzi model [16] to obtain the narrowband k-distribution of the gas mixture. Currently three radiative gas species commonly involved in coal combustion are considered, which are  $CO_2$ ,  $H_2O$  and CO. Over each narrowband, the solid absorption coefficient of each phase may be approximated by a constant value equals to its average absorption coefficient over the narrowband. Then the narrowband k-distribution of the gas-particle mixture is obtained by adding the narrowband solid absorption coefficients of all solid phases to the narrowband gas k-distribution over each narrowband [16]. The full-spectrum k-distribution of the gas-particle mixture is then compiled from the narrowband *k*-distributions of the gas-particle mixture.

Solid particle radiative properties depend on their composition, size, and local number densities. With particles sizes ranging from sub- $\mu$ m to hundreds of  $\mu$ m, and wavelengths-of-importance ranging from about 0.5–10 $\mu$ m, the radiation size parameter  $x = \pi d/\lambda$  generally covers the entire range of Mie scattering from x < 0.1 (Rayleigh scattering) to x > 1000 (large particles). For a solid particle of radius a, its spectral properties at wavenumber  $\eta$  are determined by the complex refractive index of solids **m**, the size parameter  $x = 2\pi a \eta$  and the clearance ratio. Buckius and Hwang [17] noticed that when normalized by their Rayleigh limit, the absorption and extinction coefficients are virtually independent of particle size distribution and only depend on an effective mean particle diameter. They noted that the nondimensional extinction and absorption coefficients  $(\beta^*, \kappa^*)$  may be expressed by a correlation from their Rayleigh limits as shown in Fig. 1. Then

$$\beta^{*-1.2} = [\beta_0^* (1 + 6.78 \beta_0^{*2})]^{-1.2} + (3.09/\beta_0^{*0.1})^{-1.2}$$

$$\kappa^{*-1.6} = [\beta_0^* (1 + 2.30 \beta_0^{*2})]^{-1.6} + (1.66/\beta_0^{*0.16})^{-1.6}$$
(2)

$$\kappa^{*-1.6} = [\beta_0^* (1 + 2.30 \beta_0^{*2})]^{-1.6} + (1.66 / \beta_0^{*0.16})^{-1.6}$$
(2)

where  $\beta_0^*$  denotes the Rayleigh small particle limit of a nondimensional extinction coefficient

$$\beta_0^*(\eta, \mathbf{m}) = -4\bar{x}\Im\left(\frac{\mathbf{m}^2 - 1}{\mathbf{m}^2 + 1}\right) \tag{3}$$

where  $\bar{x}$  is the size parameter based on mean particle radius and  $\Im$  denotes the imaginary part. The solid particle (linear-based) absorption and extinction coefficients are related to nondimensional values by

$$\kappa = \kappa^* f_A \text{ and } \beta = \beta^* f_A$$
 (4)

where  $f_A$  is the total area of particles per unit volume, i.e.,

$$f_A = \int_0^\infty \pi a^2 n(a) da \tag{5}$$

given the size distribution n(a).

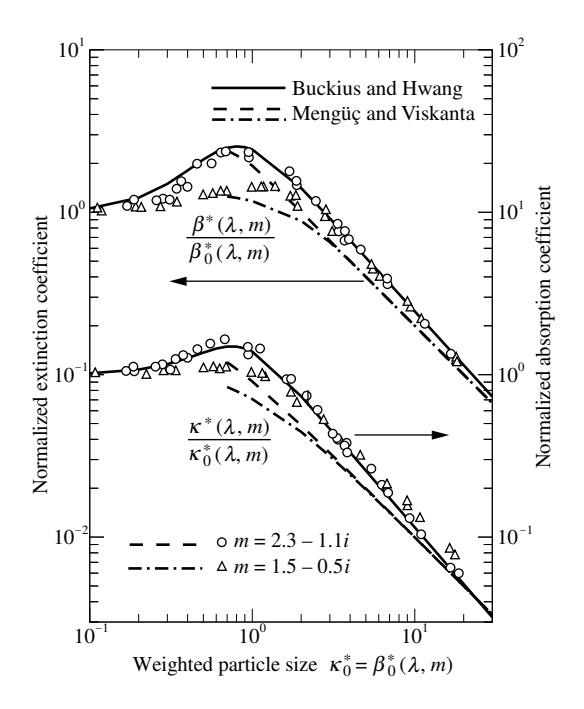


**Figure 1:** Extinction and absorption properties of pulverized coal as assembled by Buckius and Hwang [14] (subscript "0" refers to Rayleigh small-particle limit).

Impure particles are modeled as pseudo-species, e.g., fixed carbon, ash, etc. Solid spectral properties of the corresponding pure particles are calculated before weighting by the volume fractions of pseudo-species. Because narrowband absorption coefficients  $\kappa^*$  are assumed to be independent of temperature and pressure, they are databased online to save computational time on property evaluations.

A radiative property database for coal was added to the MFIX source code. The database is programmed in Fortran and is maintained as a separate module. Species are identified from database through their names. The functions in this module return the complex refractive index for each solid species at any individual wavenumber. It also returns narrowband averaged complex refractive indices needed to predict the solids' absorption and scattering properties, and is compatible with the gas phase narrowband k-distribution module. This module is only called by the solid radiative property calculation module, but is in a separate file for ease of future extension. Currently three species frequently used in coal combustion are included. Their values are listed in Table 1.

| coal composition | т            |
|------------------|--------------|
| fixed carbon     | 2.2 - 1.12i  |
| fly ash          | 1.5 - 0.02i  |
| volatile matter  | 2.05 - 0.54i |

**Table 1:** Coal composition and their complex refractive indices.

It should be noted that the generic interface is not limited constant (gray) complex refractive indices, but rather any kind of spectral variations. In order to add new solid species to the database, the user needs to first add the species name to the recognized species list and assign it an id, then add the spectral complex refractive index function into the solid radiative property database.

## 2.3 Spectral Module for Radiation in Multi-Phase Mixtures

In gas-particle flows, polydisperse particles are grouped into phases by their size and material because of distinguishing characteristics of momentum transfer. Particles of each phase also have individual dynamical responses to heat transfer, which requires a dedicated energy equation and each energy equation requires an individual radiative heat source. On the other hand, the radiation field is described by a single radiative transfer equation (RTE), which determines the total radiative heat source. Therefore, an accurate scheme is needed to split the total heat source across phases in gas-particle mixtures.

Solving the RTE requires spectral models for radiatively participating gases commonly occurring in coal combustion, such as  $CO_2$ , CO and  $H_2O$ . Their absorption coefficients have strong spectral dependency. Common particles in coal combustion include soot, coal, char, ash and limestone [18]. Their radiative properties are not gray even for gray complex refractive indices due to dependency on the size parameter [14].

While the line-by-line (LBL) spectral model [19] provides the most accurate results of radiative heat transfer, its large computational demands prevent its use in practical engineering applications. Recently, *k*-distribution methods have been developed for gases [16, 20, 21]. A *k*-distribution is a spectrally reordered absorption coefficient over a narrow-band or the full spectrum. Using *k*-distributions, radiative heat transfer can be solved with excellent accuracy, but at a small fraction of the effort compared to LBL calculations [16].

Although the total heat source can be accurately predicted using *k*-distribution methods, the reordering process makes splitting the total heat source across phases challenging because of the loss of spectral information. For example as shown in Fig. 3, for a nongray solid gas-particle mixture, multiple solid absorption coefficient values may correspond to one total absorption coefficient value. After reordering, due to the loss of spectral information, the individual solid phase absorption of radiation is indeterminate.

In this project a regression scheme was developed to extend the validity of the k-distribution scheme to multi-phase gas-particulate mixtures with multiple emission temperatures, and to accurately distribute the resulting radiative source across the phases. The new method is tested with several examples, demonstrating its validity and accuracy.

#### Theoretical Analysis

Consider a gas-particle mixture with particles grouped into M different phases according to their material and/or sizes with  $m=1,2,\ldots,M$  and in particular let m=0 be the gas phase. Particles of different size possess different radiative properties and may have different temperatures due to different reaction rates and responses to heat transfer. The spectral radiative transfer equation (RTE) of radiation intensity  $I_{\eta}$  at wavenumber  $\eta$  including absorption, scattering and multiple temperature emission for a gas-particle mixture may be stated as [14]

$$\frac{dI_{\eta}}{ds} = \sum_{m=0}^{M} \kappa_{m\eta} I_{\text{b}\eta}(T_m) - \sum_{m=0}^{M} \kappa_{m\eta} I_{\eta} - \sum_{m=0}^{M} \sigma_{\text{s}m\eta} I_{\eta} + \sum_{m=0}^{M} \left[ \sigma_{\text{s}m\eta} \frac{1}{4\pi} \int_{4\pi} I_{\eta}(\hat{s}') \Phi_{m\eta}(\hat{s}, \hat{s}', \eta) d\Omega \right]$$
(6)

where  $\kappa_{m\eta}$  are the absorption coefficient,  $I_{b\eta}$  the Planck function,  $\sigma_{sm\eta}$  the scattering coefficient and  $\Phi_{m\eta}$  the scattering phase function of phase m. Both absorption and scattering coefficients are functions of state variable arrays  $\underline{\phi}$  and  $\underline{\phi}_s$ , i.e.,  $\phi$  contains the gas properties, such as temperature, pressure and species concentration, and  $\overline{\phi}_s$  contains information of local particle properties such as particle number density, radius and species.

We now apply reordering according to the total absorption coefficient at reference state  $(\kappa_{\eta}^0)$ 

over the full spectral range [14,22]:

$$\int_{\eta} [\bullet] \delta(k - \kappa_{\eta}^{0}) d\eta \tag{7}$$

The superscript  $^0$  indicates a reference state, i.e.,  $\kappa_{\eta}^0 = \kappa_{\eta}(\underline{\phi}^0, \underline{\phi}_s^0)$  indicates the absorption coefficient at a reference state specified by state variable arrays  $\underline{\phi}^0$  and  $\underline{\phi}_s^0$ . Similar to the full spectrum k-distribution method [14], after performing the integration indicated by Eq. (7), each term in Eq. (6) is transformed (reordered) as follows:

The path derivative (term on the left) becomes

$$\int_{\eta} \frac{dI_{\eta}}{ds} \delta(k - \kappa_{\eta}^{0}) d\eta = \frac{d}{ds} \int_{\eta} I_{\eta} \delta(k - \kappa_{\eta}^{0}) d\eta = \frac{d}{ds} I_{k}$$
 (8)

where

$$I_k = \int_{\eta} I_{\eta} \delta(k - \kappa_{\eta}^0) d\eta \tag{9}$$

The emission term (first on the right) becomes

$$\int_{\eta} \sum_{m=0}^{M} \kappa_{m\eta} I_{b\eta}(T_{m}) \delta(k - \kappa_{\eta}^{0}) d\eta$$

$$= \sum_{m=0}^{M} \int_{\eta} \kappa_{m\eta} I_{b\eta}(T_{m}) \delta(k - \kappa_{\eta}^{0}) d\eta$$

$$= k_{0}^{*}(k) \int_{\eta} I_{b\eta}(T_{0}) \delta(k - \kappa_{\eta}^{0}) d\eta + \sum_{m=1}^{M} \hat{k}_{m}(k; T_{m}) \int_{\eta} I_{b\eta}(T_{m}) \delta(k - \kappa_{\eta}^{0}) d\eta$$

$$= k_{0}^{*} I_{b}(T_{0}) f_{FS}(T_{0}, \underline{\phi}^{0}, \underline{\phi}^{0}_{s}, k) + \sum_{m=1}^{M} \left[ \hat{k}_{m}(k; T_{m}) I_{b}(T_{m}) f_{FS}(T_{m}, \underline{\phi}^{0}, \underline{\phi}^{0}_{s}, k) \right] \tag{10}$$

where the gas absorption coefficients are assumed to be correlated with total absorption coefficients, i.e., there exists a map  $K_0$  [22]

$$\kappa_{0\eta}(\underline{\phi},\underline{\phi}_{s},\eta) = K_{0}(\underline{\phi},\underline{\phi}_{s},\kappa_{\eta}(\underline{\phi}^{0},\underline{\phi}_{s}^{0},\eta)) = K_{0}(\underline{\phi},\underline{\phi}_{s},\kappa_{\eta}^{0}) \tag{11}$$

which gives

$$k_0^* = K_0(\boldsymbol{\phi}, \boldsymbol{\phi}_s, k; \boldsymbol{\phi}^0, \boldsymbol{\phi}^0)$$
 (12)

The correlation assumption for a mixture of a gas with nongray particles may be examined by plotting line-by-line gas absorption coefficients against the total absorption coefficients as shown in Fig. 2, for a typical  $CO_2$ - $N_2$ -char mixture with properties given in the figure caption. The gas absorption coefficients cluster around a monotonic curve, suggesting the existence of the map  $K_0$  and the validity of correlation assumption. The correlation between gases at varying temperature and concentration has been found to be good in early work on nonluminous reacting flows [16]. Such correlation is not generally available for solid absorption coefficients as shown in Fig. 3 for the same mixture. For a given total absorption coefficient, several different solid absorption coefficients are possible. However, an apparent (or relevant average) solid absorption coefficient may be determined from a regression as

$$\hat{k}_m(k;T) = \frac{\int_{\eta} \kappa_{m\eta} I_{\text{b}\eta}(T) \delta(k - \kappa_{\eta}^0) d\eta}{\int_{\eta} I_{\text{b}\eta}(T) \delta(k - \kappa_{\eta}^0) d\eta}$$
(13)

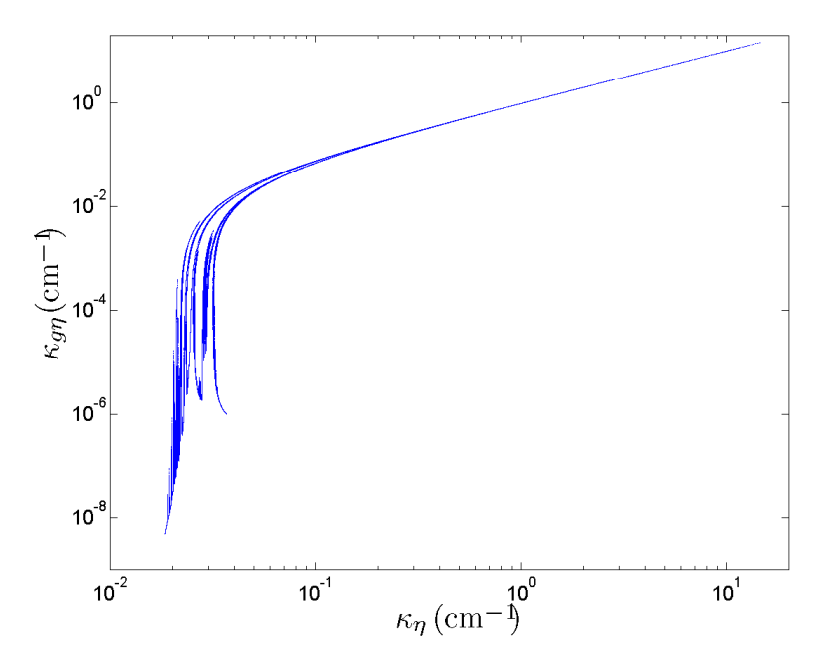


**Figure 2:** Line-by-line scatter plot of gas phase absorption coefficient ( $\kappa_{g\eta}$ ) vs total absorption coefficient ( $\kappa_{\eta}$ ). The mixture has 10% CO<sub>2</sub> and 90% N<sub>2</sub> by volume. The particles are char with a complex refractive index m = 2.2 - 1.12i and a uniform diameter of 400 μm. The volume fraction of particle is 0.001. The mixture has a temperature of 600K.

This allows us to find a proper average value of  $\kappa_{m\eta}$  that occurs in the presence of a total absorption coefficient  $\kappa_{\eta}^{0}$ . The definition of the full spectrum k-distribution for a multi-temperature mixture remains the same as its definition for a single-temperature medium:

$$f_{\rm FS}(T, \underline{\phi}^0, \underline{\phi}^0_s, k) = \frac{1}{I_{\rm b}(T)} \int_{\eta} I_{\rm b\eta}(T) \delta(k - \kappa_{\eta}^0) d\eta \tag{14}$$

The absorption term (second on the right) becomes

$$\int_{\eta} \sum_{m=0}^{M} \kappa_{m\eta} I_{\eta} \delta(k - \kappa_{\eta}^{0}) d\eta$$

$$= \int_{\eta} \kappa_{0\eta} I_{\eta} \delta(k - \kappa_{\eta}^{0}) d\eta + \sum_{m=1}^{M} \int_{\eta} \kappa_{m\eta} I_{\eta} \delta(k - \kappa_{\eta}^{0}) d\eta$$

$$= k_{0}^{*} \int_{\eta} I_{\eta} \delta(k - \kappa_{\eta}^{0}) d\eta + \sum_{m=1}^{M} \left\{ \frac{\int_{\eta} \kappa_{m\eta} I_{\eta} \delta(k - \kappa_{\eta}^{0}) d\eta}{\int_{\eta} I_{\eta} \delta(k - \kappa_{\eta}^{0}) d\eta} \right\} \int_{\eta} I_{\eta} \delta(k - \kappa_{\eta}^{0}) d\eta$$

$$\approx k_{0}^{*} I_{k} + \left[ \sum_{m=1}^{M} \hat{k}_{m} \right] I_{k} \tag{15}$$

where the term in the curly braces is approximated as

$$\frac{\int_{\eta} \kappa_{m\eta} I_{\eta} \delta(k - \kappa_{\eta}^{0}) d\eta}{\int_{\eta} I_{\eta} \delta(k - \kappa_{\eta}^{0}) d\eta} \approx \frac{\int_{\eta} \kappa_{m\eta} I_{b\eta}(T_{m}) \delta(k - \kappa_{\eta}^{0}) d\eta}{\int_{\eta} I_{b\eta}(T_{m}) \delta(k - \kappa_{\eta}^{0}) d\eta} = \hat{k}_{m}(k; T_{m})$$
(16)

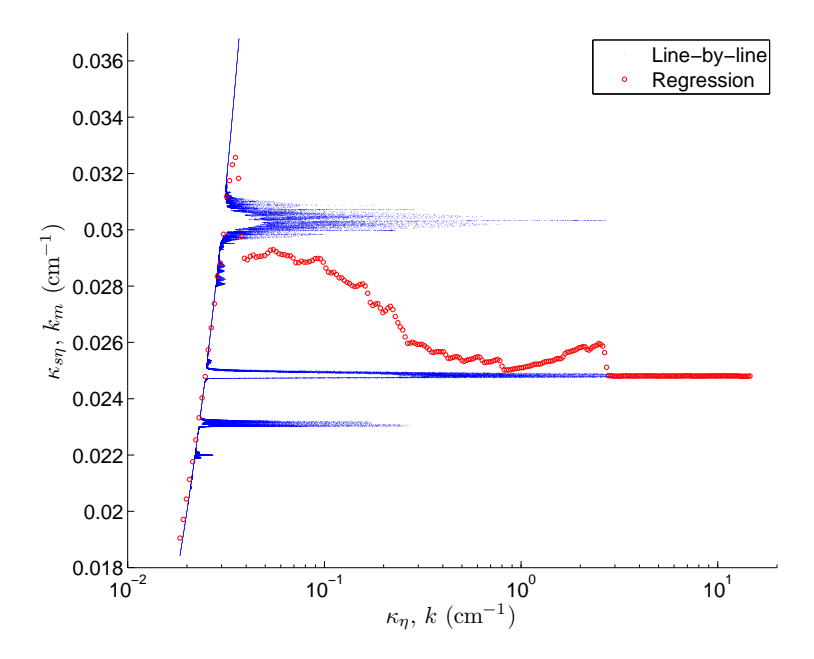


**Figure 3:** Line-by-line scatter plot of solid phase absorption coefficient ( $\kappa_{s\eta}$ ) vs total absorption coefficient ( $\kappa_{\eta}$ ). The regression of solid absorption coefficient against total absorption coefficient is shown by red circles. Mixture conditions are the same as Fig. 2

This approximation is equivalent to assuming that  $I_{\eta} \propto I_{b\eta}(T_m)$  over the spectrum. The proportionality factor may vary with space and direction. For example, if space and spectral dependence are separable

$$I_{\eta}(\underline{x}, \hat{s}, \eta) = p(\underline{x}, \hat{s})I_{b\eta}(T_m) \tag{17}$$

Eq. (16) is still exact when p is not a function of wavenumber. Eq. (17) is valid in an isothermal homogeneous mixture bounded by cold black walls, or for a medium with a scaled absorption coefficient. Deviations may arise near a wall with a different temperature, in the presence of strong temperature gradients and if phase temperatures are very different.

The treatment of scattering will follow Modest and Riazzi [16], in which they demonstrated that gray scattering coefficients ( $\sigma_{sm\eta} = \sigma_{sm}$ ) and phase functions ( $\Phi_{m\eta} = \Phi_m$ ) are valid approximations even for extremely nongray scatterers. By dropping spectral dependence in scattering properties and reordering according to Eq. (7), the scattering terms become

$$\int_{\eta} \left\{ \sum_{m=0}^{M} \sigma_{sm\eta} I_{\eta} + \sum_{m=0}^{M} \left[ \sigma_{sm\eta} \frac{1}{4\pi} \int_{4\pi} I_{\eta}(\hat{s}') \Phi_{m\eta}(\hat{s}, \hat{s}', \eta) d\Omega \right] \right\} \delta(k - \kappa_{\eta}^{0}) d\eta$$

$$= \sum_{m=0}^{M} \sigma_{sm} I_{k} + \sum_{m=0}^{M} \left[ \sigma_{sm} \frac{1}{4\pi} \int_{4\pi} \Phi_{m}(\hat{s}, \hat{s}') I_{k}(\hat{s}') d\Omega \right]$$
(18)

Assuming gas phase scattering to be negligible, the summation over phases starts from m = 1.

Combining the above terms, the reordered RTE becomes

$$\frac{dI_{k}}{ds} = k_{0}^{*}(k)I_{b}(T_{0})f_{FS}(T_{0},\underline{\phi}^{0},\underline{\phi}^{0}_{s},k) + \sum_{m=1}^{M} \left[\hat{k}_{m}(k;T_{m})I_{b}(T_{m})f_{FS}(T_{m},\underline{\phi}^{0},\underline{\phi}^{0}_{s},k)\right] \\
- \left[k_{0}^{*}(k) + \sum_{m=1}^{M} \hat{k}_{m}(k;T_{m})\right]I_{k} - \sum_{m=1}^{M} \sigma_{sm}I_{k} + \sum_{m=1}^{M} \left[\sigma_{sm}\frac{1}{4\pi} \int_{4\pi} \Phi_{m}(\hat{s},\hat{s}')I_{k}(\hat{s}')d\Omega\right] \quad (19)$$

Defining the cumulative *k*-distribution as

$$g(k; T^0, \underline{\phi}^0, \underline{\phi}^0) = \int_0^k f_{FS}(T^0, \underline{\phi}^0, \underline{\phi}^0, k') dk'$$
(20)

and

$$I_g(g(k), \underline{r}, \hat{s}) = I_k(k, \underline{r}, \hat{s}) / f_{FS}(T^0, \underline{\phi}^0, \underline{\phi}^0, k)$$
(21)

where  $T^0$  is the reference temperature and  $T_0$  the gas phase temperature. The new RTE for  $I_g$  becomes

$$\frac{dI_g}{ds} = k_0^*(g)a(T_0, T^0, g)I_b(T_0) + \sum_{m=1}^M \hat{k}_m(g; T_m)a(T_m, T^0, g)I_b(T_m) - \left[k_0^*(g) + \sum_{m=1}^M \hat{k}_m(g; T_m)\right]I_g$$

$$- \sum_{m=1}^M \sigma_{sm}I_g + \sum_{m=1}^M \left[\sigma_{sm}\frac{1}{4\pi} \int_{4\pi} \Phi_m(\hat{s}, \hat{s}')I_g(\hat{s}')d\Omega\right] \quad (22)$$

where the nongray stretching function a is defined as

$$a(T_m, T^0, g) = \frac{f_{FS}(T_m, \underline{\phi}^0, \underline{\phi}^0, k(g))}{f_{FS}(T^0, \underline{\phi}^0, \underline{\phi}^0, k(g))}$$
(23)

To split the heat source across phases, one may use the same assumption as in the derivation of the absorption term in the RTE for solid phases as given by Eq. (16). The heat source for solid

phase  $m (m \ge 1)$  then becomes

$$S_{m} = -\nabla \cdot \mathbf{q}_{m} = -\int_{\eta} \nabla \cdot \mathbf{q}_{m\eta} d\eta$$

$$= \int_{4\pi} \int_{\eta} \kappa_{m\eta} I_{\eta} d\eta d\Omega - 4\pi \int_{\eta} \kappa_{m\eta} I_{b\eta} d\eta$$

$$= \int_{4\pi} \int_{\eta} \kappa_{m\eta} I_{\eta} \int_{k=0}^{\infty} \delta(k - \kappa_{\eta}^{0}) dk d\eta d\Omega - 4\pi \kappa_{Pm} I_{b}(T_{m})$$

$$= \int_{4\pi} \int_{k=0}^{\infty} \int_{\eta} \kappa_{m\eta} I_{\eta} \delta(k - \kappa_{\eta}^{0}) d\eta dk d\Omega - 4\pi \kappa_{Pm} I_{b}(T_{m})$$

$$\approx \int_{4\pi} \int_{k=0}^{\infty} \hat{k}_{m}(k; T_{m}) \int_{\eta} I_{\eta} \delta(k - \kappa_{\eta}^{0}) d\eta dk d\Omega - 4\pi \kappa_{Pm} I_{b}(T_{m})$$

$$= \int_{k=0}^{\infty} \hat{k}_{m}(k; T_{m}) \int_{4\pi} I_{k} d\Omega dk - 4\pi \kappa_{Pm} I_{b}(T_{m})$$

$$= \int_{k=0}^{\infty} \hat{k}_{m}(k; T_{m}) G_{k} dk - 4\pi \kappa_{Pm} I_{b}(T_{m})$$

$$= \int_{q=0}^{1} \hat{k}_{m}(k; T_{m}) G_{g} dg - 4\pi \kappa_{Pm} I_{b}(T_{m})$$

$$(24)$$

The gas phase heat source is, assuming the gas to be correlated,

$$S_{0} = -\nabla \cdot \boldsymbol{q}_{0} = -\int_{\eta} \nabla \cdot \boldsymbol{q}_{0\eta} d\eta$$

$$= \int_{4\pi} \int_{\eta} \kappa_{0\eta} I_{\eta} d\eta d\Omega - 4\pi \int_{\eta} \kappa_{0\eta} I_{b\eta} d\eta$$

$$= \int_{4\pi} \int_{\eta} \kappa_{0\eta} I_{\eta} \int_{k=0}^{\infty} \delta(k - \kappa_{\eta}^{0}) dk d\eta d\Omega - 4\pi \kappa_{P0} I_{b}(T_{0})$$

$$= \int_{4\pi} \int_{k=0}^{\infty} \int_{\eta} \kappa_{0\eta} I_{\eta} \delta(k - \kappa_{\eta}^{0}) d\eta dk d\Omega - 4\pi \kappa_{P0} I_{b}(T_{0})$$

$$= \int_{4\pi} \int_{k=0}^{\infty} k_{0}^{*} \int_{\eta} I_{\eta} \delta(k - \kappa_{\eta}^{0}) d\eta dk d\Omega - 4\pi \kappa_{P0} I_{b}(T_{0})$$

$$= \int_{k=0}^{\infty} k_{0}^{*}(k) \int_{4\pi} I_{k} d\Omega dk - 4\pi \kappa_{P0} I_{b}(T_{0})$$

$$= \int_{k=0}^{\infty} k_{0}^{*}(k) G_{k} dk - 4\pi \kappa_{P0} I_{b}(T_{0})$$

$$= \int_{k=0}^{1} k_{0}^{*}(k) G_{k} dk - 4\pi \kappa_{P0} I_{b}(T_{0})$$

$$= \int_{q=0}^{1} k_{0}^{*}(k) G_{g} dg - 4\pi \kappa_{P0} I_{b}(T_{0})$$

$$(25)$$

The total heat source is obtained by integrating Eq. (22) over all solid angles and all g, and is

conserved because

$$\sum_{m=0}^{M} S_{m} = \int_{0}^{1} \left[ k_{0}^{*}(k(g)) + \sum_{m=1}^{M} \hat{k}_{m}(k(g); T_{m}) \right] G_{g} dg - \sum_{m=0}^{M} 4\pi \kappa_{Pm} I_{b}(T_{m})$$

$$= \int_{0}^{1} \left[ k_{0}^{*}(g) + \sum_{m=1}^{M} \hat{k}_{m}(g) \right] G_{g} dg$$

$$- 4\pi \int_{g=0}^{1} k_{0}^{*}(g) a_{0}(g) I_{b}(T_{0}) dg - 4\pi \sum_{m=1}^{M} \int_{0}^{1} \hat{k}_{m}(g) a_{m}(g) I_{b}(T_{m}) dg$$

$$= \int_{0}^{1} \left\{ \left[ k_{0}^{*}(g) + \sum_{m=1}^{M} \hat{k}_{m}(g) \right] G_{g} - 4\pi \left[ k_{0}^{*}(g) a_{0}(g) I_{b}(T_{0}) + \sum_{m=1}^{M} \hat{k}_{m}(g) a_{m}(g) I_{b}(T_{m}) \right] \right\} dg$$

$$= -\int_{0}^{1} \nabla \cdot \mathbf{q}_{g} dg = -\nabla \cdot \mathbf{q} \tag{26}$$

**Regression** To calculate the full-spectrum k-distribution of a gas-particle mixture, we use databased narrowband k-distributions [15] of the combustion gases and mix them based on the Modest-Riazzi model [16] to obtain the narrowband k-distribution of the gas mixture. Over each narrowband, the solid absorption coefficient of each phase may be approximated by a constant value equal to its average absorption coefficient over the narrowband. Then the narrowband k-distribution of the gas-particle mixture is obtained by adding the narrowband solid absorption coefficients of all solid phases to the narrowband gas k-distribution over each narrowband [16]. The full-spectrum k-distribution of the gas-particle mixture is then compiled from the narrowband k-distributions of the gas-particle mixture.

The regression of solid absorption coefficient in Eq. (13) is calculated with narrowband k-distributions of the mixture. Suppose that the spectrum is partitioned into  $N_{NB}$  narrowbands and the particle absorption coefficient of phase m is approximated by a constant value  $k_{m,n}$  over the nth narrowband. Over this narrowband, the cumulative k-distribution of the gas-particle mixture is  $g_{n,i}$  for a sequence of increasing  $k_i$ s ( $i = 1, 2, ..., N_i$ , where  $N_i$  is the total number of k values). The regression  $\hat{k}_m$  is expressed as a weighted average of  $k_{m,n}$  from all narrowbands with the weights proportional to the narrowband k-distributions and the narrowband integral Planck function, i.e.,

$$\hat{k}_{m}(k_{i}) = \frac{\int_{\eta} I_{b\eta} \kappa_{m\eta} \delta(k_{i} - \kappa_{\eta}) d\eta}{\int_{\eta} I_{b\eta} \delta(k_{i} - \kappa_{\eta}) d\eta} \approx \frac{\int_{(k_{i} + k_{i-1})/2}^{(k_{i} + k_{i-1})/2} \int_{\eta} I_{b\eta} \kappa_{m\eta} \delta(k - \kappa_{\eta}) d\eta dk}{\int_{(k_{i} + k_{i-1})/2}^{(k_{i} + k_{i-1})/2} \int_{\eta} I_{b\eta} \delta(k - \kappa_{\eta}) d\eta dk}$$

$$(27)$$

The numerator may be expressed as

$$\begin{split} & \int_{(k_{i}+k_{i-1})/2}^{(k_{i}+k_{i+1})/2} \int_{\eta} I_{b\eta} \kappa_{m\eta} \delta(k-\kappa_{\eta}) d\eta dk \\ & = \int_{\eta} \int_{(k_{i}+k_{i+1})/2}^{(k_{i}+k_{i+1})/2} I_{b\eta} \kappa_{m\eta} \delta(k-\kappa_{\eta}) dk d\eta \\ & = \sum_{n=1}^{N_{\text{NB}}} \int_{\eta_{n}}^{\eta_{n}+\Delta \eta_{n}} \int_{(k_{i}+k_{i-1})/2}^{(k_{i}+k_{i+1})/2} I_{b\eta_{n}} \kappa_{m\eta_{n}} \delta(k-\kappa_{\eta}) dk d\eta \end{split}$$

$$= \sum_{n=1}^{N_{NB}} I_{b\eta_{n}} \kappa_{m\eta_{n}} \int_{\eta_{n}}^{\eta_{n}+\Delta\eta_{n}} \int_{(k_{i}+k_{i+1})/2}^{(k_{i}+k_{i+1})/2} \delta(k-\kappa_{\eta}) dk d\eta$$

$$= \sum_{n=1}^{N_{NB}} I_{b\eta_{n}} \Delta \eta \kappa_{m,n} \int_{(k_{i}+k_{i+1})/2}^{(k_{i}+k_{i+1})/2} \frac{1}{\Delta \eta} \int_{\eta_{n}}^{\eta_{n}+\Delta\eta_{n}} \delta(k-\kappa_{\eta}) d\eta dk$$

$$= \sum_{n=1}^{N_{NB}} I_{bn} \kappa_{m,n} \int_{(k_{i}+k_{i+1})/2}^{(k_{i}+k_{i+1})/2} \frac{1}{\Delta \eta} \int_{\eta_{n}}^{\eta_{n}+\Delta\eta_{n}} \delta(k-\kappa_{\eta}) d\eta dk$$

$$= \sum_{n=1}^{N_{NB}} I_{bn} \kappa_{m,n} \int_{(k_{i}+k_{i+1})/2}^{(k_{i}+k_{i+1})/2} f_{NB}(k;n) dk$$

$$= \sum_{n=1}^{N_{NB}} I_{bn} \kappa_{m,n} \Delta g_{i,n}$$
(28)

where  $\kappa_{m,n}$  is the constant solid phase absorption coefficient of phase m over narrowband n,  $I_{\mathrm{b}n} = \int_{\eta_n}^{\eta_n + \Delta \eta_n} I_{\mathrm{b}\eta} d\eta$  is the fraction of Planck function over narrowband n,  $f_{\mathrm{NB}}(k;n)$  is the narrowband k-distribution at k over narrowband k-distribution around k-distribu

$$\int_{(k_i+k_{i-1})/2}^{(k_i+k_{i+1})/2} \int_{\eta} I_{b\eta} \delta(k-\kappa_{\eta}) d\eta dk = \sum_{n=1}^{N_{NB}} I_{bn} \Delta g_{i,n}$$
 (29)

Combining Eqs. (28) and (29), the regression may be evaluated as

$$\hat{k}_{m}(k_{i}) = k_{m,i} = \frac{\sum_{n=1}^{N_{NB}} I_{bn} \kappa_{m,n} \Delta g_{i,n}}{\sum_{n=1}^{N_{NB}} I_{bn} \Delta g_{i,n}}$$
(30)

This model is implemented based on the narrowband k-distribution database for common radiatively participating gases in combustion [15, 23]. The gas spectra between  $200 \text{cm}^{-1}$  and  $15000 \text{cm}^{-1}$  are divided into 248 narrowbands. The solid phase absorption coefficient over each narrowband is approximated by its average value across each narrowband. After adding the narrowband constant solid phase absorption coefficients to the mixture narrowband k-distributions, the regression is evaluated using equation (30) while the narrowband k-distribution of the mixture is compiled into its full-spectrum counterpart [15].

A sample regression is included in Fig. 3, in which 256 k values are used, with the corresponding  $\hat{k}_m$  marked by circles. Note that for small k values, gas absorption is negligible, and the  $\hat{k}_m$  takes the same value as k. For large k values ( $k > 3 \text{cm}^{-1}$ ), the total absorption coefficient is dominated by gas absorption at the line centers, and  $\hat{k}_m$  approaches the solid absorption coefficient at the corresponding wavenumber.

# Sample calculations

First consider the radiation in a homogeneous gas-particle field bounded by two parallel black cold walls. The gas phase has 10% CO<sub>2</sub> and 90% N<sub>2</sub>. The particles are char with a complex refractive index m = 2.2 - 1.12i [24] and a uniform diameter of  $400\mu$ m. The volume fraction of the particles is 0.001. The mixture slab has a temperature of 600K and a thickness of 7cm. The gray scattering coefficient is evaluated at the wavenumber where the Planck function peaks and scattering is assumed to be isotropic. The gas absorption coefficient is calculated from databased

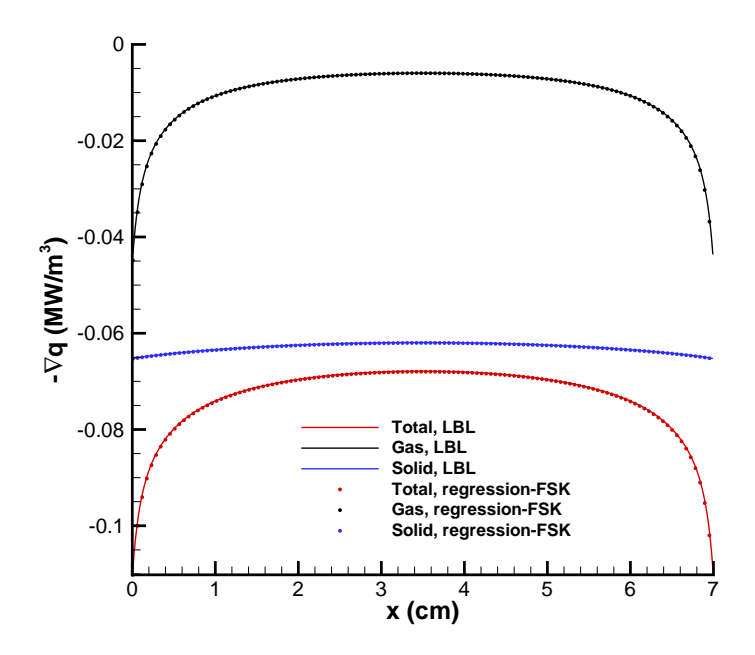


**Figure 4:** Heat source calculation of an homogeneous slab between line-by-line (solid lines) and full-spectrum *k*-distribution with regression (dots). Line colors are red (total heat source), black (gas phase heat source) and blue (solid phase heat source).

narrowband *k*-distributions and the solid absorption coefficient is approximated as constant across each narrowband [16].

Equation (22) is solved with the  $P_1$  approximation using 64 quadrature points for g. The results of total, gas and solid phase radiative heat sources are compared with line-by-line calculations in Fig. 4. The k-distribution method is capable of predicting all of the heat sources accurately (to within 1%).

To demonstrate the accuracy of the regression method in inhomogeneous media, one-dimensional slabs, bounded by two parallel black cold walls are considered. The slabs have two homogeneous gas-particle mixture layers with equal thickness. For all five inhomogeneous test cases, the left layer has a solid temperature of 500K, a gas temperature of 600K and a  $CO_2$  mole fraction of 5% diluted by  $O_2$  and  $N_2$ , while the right layer has a solid temperature of 500K, a gas temperature of 1200K and a  $CO_2$  mole fraction of 10% diluted by  $O_2$  and  $N_2$ .  $CO_2$  is assumed to be the only radiatively participating gas species, which reduces errors from k-distributions since only temperature levels (as opposed to concentration) contribute to uncorrelation. The inaccuracy hereby primarily comes from the approximation in Eq.(16). In both layers the particles are char with a complex refractive index m = 2.2 - 1.12i. The particle volume fractions and sizes are listed in Table 2. These configurations approximate both unburned and burning gas-particle environments in typical pulverized and both fixed and circulating fluidized-bed coal combustion conditions. For large particle volume fractions, the test layer thicknesses are reduced due to large optical thicknesses.

For all five inhomogeneous test cases, the reference states are evaluated with the method proposed by Modest [22] using only gas phase absorption coefficients, i.e., the reference state does not have particles. All results suggest that the proposed regression is not sensitive to the particle volume fractions in the choice of reference state. The correlation assumption for the total

absorption coefficients does not pose additional severe constraints upon the correlation assumption proposed for the gas phase previously [22]. This is largely due to the fact that solid phase absorption coefficients have much smaller spectral variations than gases. As a result, the gas phase absorption coefficient is well correlated with the total absorption coefficients, e.g. Fig 2. The uncorrelatedness in the solid phase absorption coefficient is approximately accounted for by the proposed regression model.

|      | Left   |        |                    | Right  |        |                      |
|------|--------|--------|--------------------|--------|--------|----------------------|
| Case | l (cm) | d (μm) | $f_v$              | l (cm) | d (μm) | $f_v$                |
| A    | 5      | 200    | 0.001              | 5      | 100    | $2.5 \times 10^{-4}$ |
| В    | 5      | 2      | $1 \times 10^{-4}$ | 5      | 0.4    | $4 \times 10^{-6}$   |
| C    | 5      | 20     | 0.001              | 5      | 8      | $1 \times 10^{-4}$   |
| D    | 0.5    | 600    | 0.6                | 0.5    | 400    | 0.05                 |
| E    | 0.5    | 600    | 0.3                | 0.5    | 400    | 0.1                  |

**Table 2:** Test configurations for inhomogeneous media: layer thickness(l), particle diameter (d) and particle volume fraction ( $f_v$ )

Equation (22) is solved with the  $P_1$  approximation using 64 quadrature points for g. The results of total, gas and solid phase radiative heat sources are compared with line-by-line calculations in Fig. 5-7. The k-distribution method is capable of predicting major trends of total and phase-split heat source terms (Fig. 5). In particular, the gas phase heat source is predicted accurately (mostly within 5%) in spite of the fact that it is at least one order less in magnitude than the total heat source. This is because gas radiation primarily comes from strong bands, and the proposed regression scheme successfully picks the solid absorption coefficients at the corresponding wavenumbers (e.g. large k values in Fig. 3). Accurate predictions of the gas phase radiative heat source terms are important for gas phase combustion because of much less gas phase volumetric specific heat. For the solid phase heat source (Fig. 5), the largest deviation occurs near the interface between the two layers. Equation (16) is greatly challenged by the sharp temperature gradient at the interface. In the left (cold) layer, the spectral incident radiation deviates significantly from the emission spectrum at the local temperature because of the emission from the hot layer. Away from the interface, such deviation is reduced and accuracy improves. However, this effect is hardly observed in the hot layer because emission from the cold layer is negligible. In the hot layer, the error is less than 1%, which is due to the temperature difference between gas and solid phases. Such deviation becomes smaller in more realistic situations (Fig. 6 and 7).

For pulverized coal cases (Fig 6, the left layer has a larger particle volume fraction and thus a larger optical thickness. Strong absorption inside of this layer by both gas and solid phase causes the radiative heat sources to decay to zero within a few centimeters, e.g.,  $-\nabla \cdot q$  is close to zero near x = 2cm (3cm away from the temperature jump). The gas phase radiative heat source is at least an order of magnitude smaller than the solid phase radiative heat source, and therefore, the solid radiative heat source is nearly equal to the total radiative heat source. Even so, the regression model successfully recovers the gas radiative heat source.

The proposed model is more successful at higher solid volume fractions as found in fluidized beds, as shown in Fig 7. Because of the increased solid absorption coefficients, the gas radiative heat source is two orders of magnitude less than that of the solid, causing the total and solid radiative heat sources to overlap. Again, even in these extreme cases, the proposed regression model is capable of predicting gas radiative heat sources accurately. Note that inside the left layer, due to large solid absorption coefficients, the radiation effect decays within a few millimeter from the temperature jump (e.g. at x = 0.2cm). Therefore, the test case layer thickness appropriate

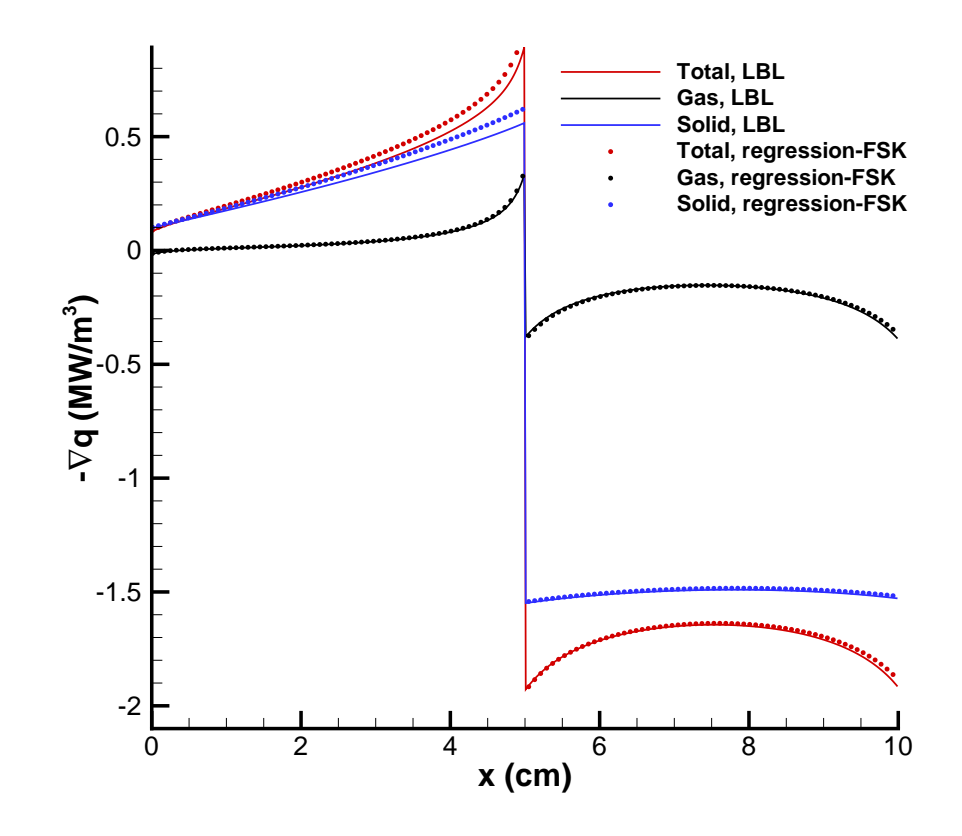


**Figure 5:** Heat source calculation of Case A between line-by-line (solid lines) and full-spectrum *k*-distribution with regression (dots). Line colors are red (total heat source), black (gas phase heat source) and blue (solid phase heat source).

for fluidized bed configurations are reduced to 0.5cm from 5cm for the pulverized coal cases. Nevertheless, the accuracy of the proposed model is improved in a dense particle flow as indicated by the overlap of regression model predictions and line-by-line predictions. This is because a larger optical thickness causes the local radiation intensity to be closer to the local Planck function, and improves the accuracy of approximation in equation (16).

The cpu time cost of k-distribution evaluations involving one participating gas species and one solid phase is 0.59s per cell, which involves two k-distribution compilations from the narrowband database, one for the local temperature and the other for the reference temperature. The one-time global evaluation of the k-distributions for the reference states is negligible when the number of mesh cells is large. Most cpu time is used to interpolate between gas narrowband k-distributions, assemble narrowband to full-spectrum k-distributions. The solid phase property and regression calculations (equation 30) add less than 1% overhead.

Although the test cases involve only one solid phase, it should be noted that all theoretical derivations are presented for an arbitrary number of solid phases. For example, all derivations assume multiple solid phases as indicated in the subscript m. The regression calculations are with respect to the total narrowband k-distributions after all solid phase narrowband absorption coefficients have been added. The scenarios for multiple solid phases are the same as for a single solid phase, making extensions to more than one solid phase straightforward. Its accuracy is

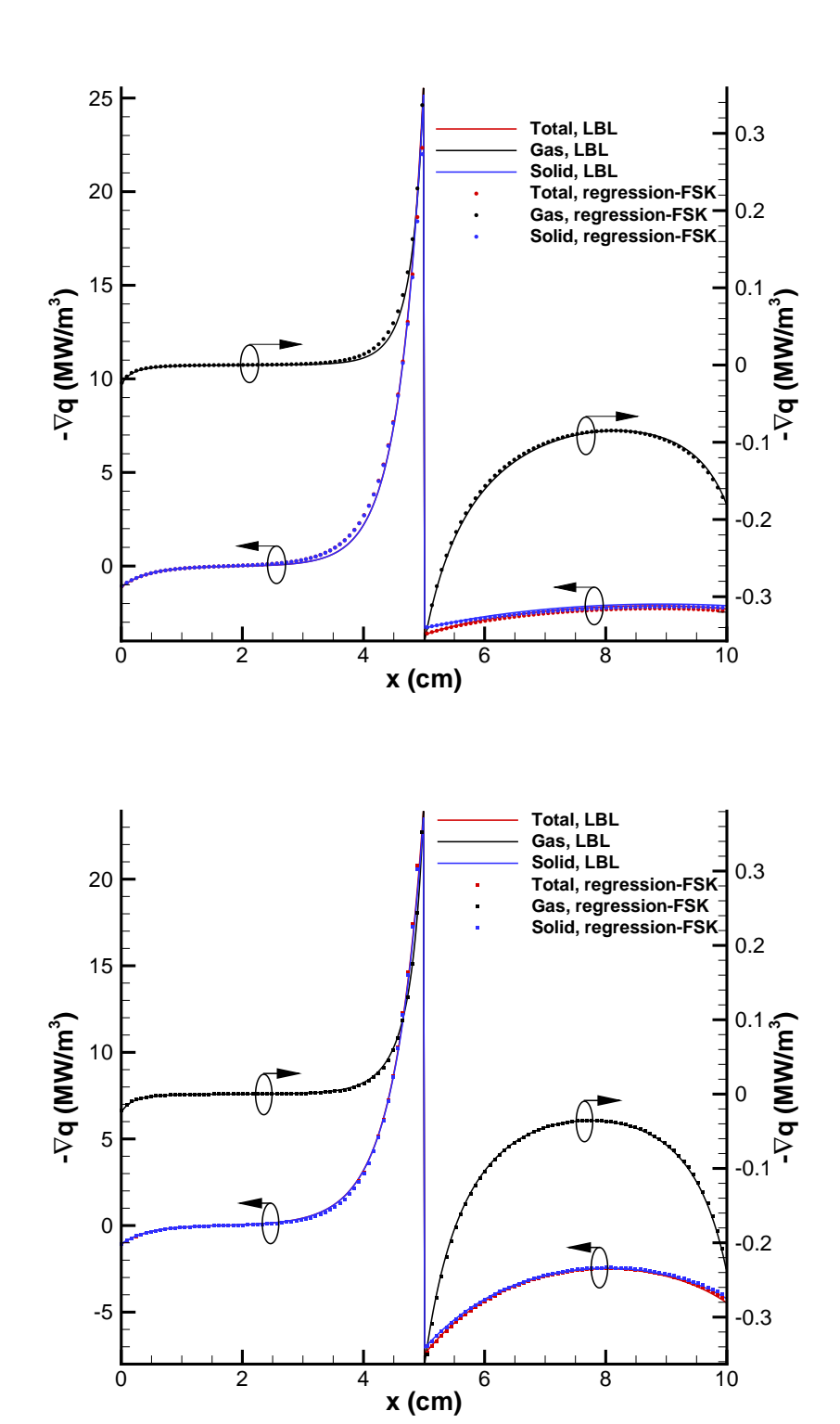


**Figure 6:** Heat source calculation of Cases B (top) and C (bottom) between line-by-line (solid lines) and full-spectrum *k*-distribution with regression (dots). Line colors are red (total heat source), black (gas phase heat source) and blue (solid phase heat source).

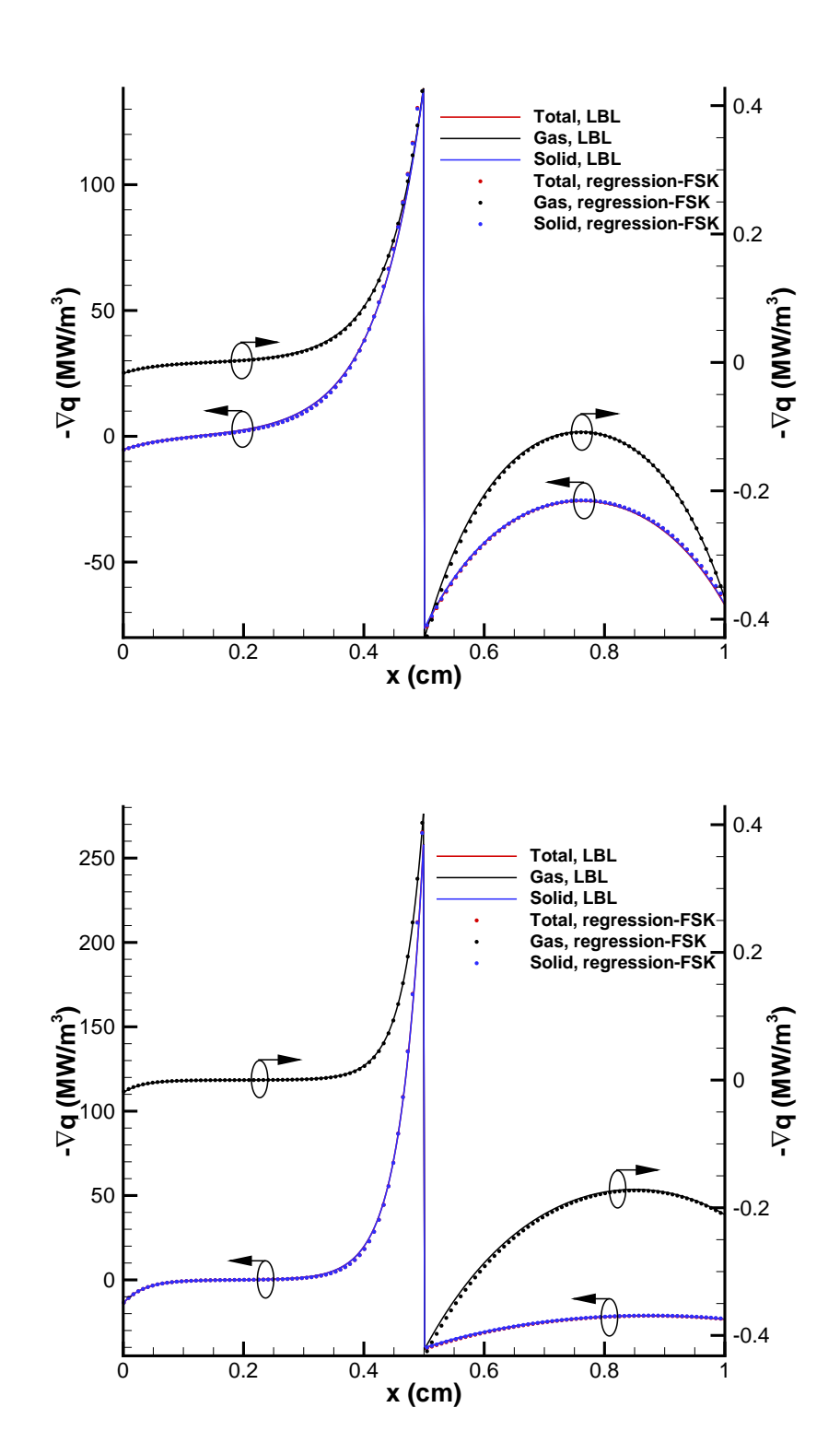


**Figure 7:** Heat source calculation of Cases D (top) and E (bottom) between line-by-line (solid lines) and full-spectrum *k*-distribution with regression (dots). Line colors are red (total heat source), black (gas phase heat source) and blue (solid phase heat source).

determined only by the correlation assumption and equation (16), e.g., the departure of local incident radiation from blackbody emission.

## 2.4 Photon Monte Carlo with Energy Splitting Across Phases for Gas-Particle Mixtures

A line-by-line photon Monte Carlo (LBL-PMC) scheme developed by Wang and Modest [25], and later improved for computational efficiency by Ren and Modest [26], is the basis for the current work. Although this LBL-PMC scheme has been applied for problems including soot radiation [27], the previous LBL-PMC models did not account for energy splitting across phases and have not been extended to include radiation with larger solid particles. This section introduces a LBL-PMC scheme, which incorporates emission and absorption energy splitting across gas particle phases, and correlations for random number relations for solid particles.

## Overview of LBL-PMC energy splitting scheme

The objective of the Photon Monte Carlo (PMC) method is to determine the absorbed radiation by a participating medium by statistically simulating the process of radiative transfer using photon bundles. Photon bundles are emitted with an assigned energy that is proportional to the local emission potential in each of the cells where they are emitted from. The directions and emission points of the rays are selected randomly within each cell of the domain. During tracing, a ray's energy is diminished according to the absorption potential of the cells that the ray traverses. Once a ray's energy is depleted, another photon bundle is emitted and is traced, and so on. After the tracing of all photon bundles is completed, the divergence of the radiative heat flux as it appears in the overall energy equation is calculated as  $\nabla \cdot \mathbf{q}_{\rm rad} = Q_{\rm emi}^{\prime\prime\prime} - Q_{\rm abs}^{\prime\prime\prime}$ , which is the emission minus the absorption on a per volume basis. This LBL-PMC implementation has several extensions to conventional LBL-PMC models employed for single gas phase media. Procedures of this extended LBL-PMC scheme include: Emission splitting, absorption splitting, an extended wavenumber selection to include solid phases, and random number relations for solid particles. Details of these procedures are presented in the following sections, followed by numerical results.

#### **Emission**

The total emission from a medium,  $Q_{\text{emi}}$ , is equal to the sum of the emission from the gas  $Q_{\text{emi},g}$  and the solid phases  $Q_{\text{emi},sm}$ . These quantities are computed on a cell basis as

$$Q_{\text{emi},i} = Q_{\text{emi},g,i} + \sum_{m=1}^{N_s} Q_{\text{emi},s,m,i},$$
(31)

where

$$Q_{\text{emi},(g)\text{or}(s,m),i} = 4\pi\bar{\kappa}_{(g)\text{or}(s,m),i}I_b(T_{(g)\text{or}(s,m),i})V_i, \tag{32}$$

(33)

where the  $\bar{\kappa}$  are Planck-mean absorption coefficients,  $N_s$  is the number of solid phases,  $V_i$  is the cell volume, and  $I_b$  are the Planck function blackbody intensities ( $I_b = \sigma T^4/\pi$ ). The Planck-mean absorption coefficient for the gas phase is obtained by summing the Planck-mean absorption coefficients of the individual gas species according to

$$\bar{\kappa}_g = \left(\sum_{n=1}^{N_g} x_n \bar{\kappa}_{g,n}\right) p_g \varepsilon_g. \tag{34}$$

where  $\bar{\kappa}_{g,n}$  and  $x_n$  are, respectively, the Planck-mean absorption coefficient and the mole fraction of the nth gas species,  $p_g$  is the total gas pressure,  $\varepsilon_g$  is the gas volume fraction, and  $N_g$  is the number of

species. The Planck-mean absorption coefficient for solids is calculated from correlations derived later in this report.

Since emission does not depend on ray tracing, there is no uncertainty directly related to the PMC for computing the emission components. Therefore, the emission field is computed prior to the start of ray tracing.

The number of photon bundles emitted from cell  $c_i$  is determined by

$$N_{r,i} = \frac{Q_{\text{emi},i}}{Q_{\text{emi}}} N_{\text{tot}}$$
(35)

where  $Q_{\text{emi}}$  is the total emission of the medium  $Q_{\text{emi}} = \sum_{i=1}^{N_i} Q_{\text{emi},i}$ , where  $N_i$  is the total number of cells, and  $N_{\text{tot}}$  is a predetermined total number of photon bundles emitted from throughout the entire medium. The uncertainty in the PMC calculations can be reduced by increasing  $N_{\text{tot}}$ .

The emission for each phase is accounted for by dividing  $N_{r,i}$  over each phase. The sum of the number of photon bundles emitted by each phase,  $N_{r,g,i}$  (number of photon bundles from the gas-phase) and  $N_{r,s,m,i}$  (number of photon bundles from the mth solid-phase), must satisfy, on a cell basis,

$$N_{r,i} = N_{r,g,i} + \sum_{m=1}^{N_s} N_{r,s,m,i}$$
(36)

If Eqn. (31) is multiplied by  $N_{r,i}/Q_{\text{emi},i}$ , then

$$N_{r,i} = \frac{Q_{\text{emi},g,i}}{Q_{\text{emi},i}} N_{r,i} + \sum_{m=1}^{N_s} \frac{Q_{\text{emi},s,m,i}}{Q_{\text{emi},i}} N_{r,i}.$$
 (37)

By comparing this equation with Eqn. (36), it is found that the appropriate partitioning of emission across phases is accomplished by emitting  $N_{r,g,i}$  gas-phase photon bundles and  $N_{r,s,m,i}$  solid-phase photon bundles according to

$$N_{r,(g)\text{or}(s,m),i} = \frac{Q_{\text{emi},(g)\text{or}(s,m),i}}{Q_{\text{emi},i}} N_{r,i},$$
(38)

which must be rounded (and the  $Q_{\text{emi},(g)\text{or}(s,m),i}$  corresponding adjusted) because  $N_{r,g,i}$  and  $N_{r,s,m,i}$  are integers.

For optimal statistical sampling, photon bundles emitted from a given cell are assigned equal amounts of energy according to

$$Q_{i}^{k} = \frac{Q_{\text{emi},g,i}}{N_{r,g,i}} = \frac{Q_{\text{emi},s,m,i}}{N_{r,s,m,i}} = \frac{Q_{\text{emi},i}}{N_{r,i}},$$
(39)

where each equality holds as a result of Eqn. (38).

In an enclosed medium there are generally two sources of emission, 1) emission from the medium and 2) emission from the wall. Photon bundles emitted from wall faces must be included in the ray tracing scheme. The emission from a wall face is calculated as

$$Q_{\text{emi},w,i} = \varepsilon_{w,i} \sigma A_{w,i} T_{w,i}^4. \tag{40}$$

where  $\varepsilon_{w,i}$ ,  $A_{w,i}$ , and  $T_{w,i}$  are respectively the wall face emittance, surface area, and temperature. The number of photons emitted by the wall faces follows a similar procedure as for the cell photons. The energy of a photon bundle emitted from a wall is computed as,

$$Q_i^k = \frac{Q_{\text{emi},w,i}}{N_{r,w,i}},\tag{41}$$

where  $N_{r,w,i}$  is proportional to the wall emission of the face,

$$N_{r,w,i} = \frac{Q_{\text{emi},w,i}}{Q_{\text{emi},\text{total}}} N_{\text{tot}}.$$
(42)

The photon bundles emitted from the wall faces are traced in the same manner as the photon bundles emitted by interior cells.

#### Wavenumber selection

This implementation of PMC adopts the line-by-line (LBL) spectral scheme that was developed by Ren and Modest [26] for gas mixtures. This LBL scheme is referred to here as the Hybrid Selection Scheme (HSS) because it involves deterministically selecting an emitting gas species, then determining wavenumbers based on gas species random number relations of the selected gas species. Following this approach of independence of emission for all species and phases, emission wavelengths for solid phases are determined independently.

The procedure of the HSS consists of the following steps:

- 1. Select a random number  $R_{n,i}^k$  for each ray in a cell.
- 2. From that random number, select the emitting species, denoted by subscript  $n^*$ , according to the condition,

$$\frac{\sum_{n=1}^{n^*-1} E_n}{E_{tot}} < R_{\eta,i}^k \le \frac{\sum_{n=1}^{n^*} E_n}{E_{tot}}$$
(43)

where

$$E_n = \int_0^\infty \kappa_{\eta,g,n} I_{b\eta} \mathrm{d}\eta \tag{44}$$

and

$$E_{\text{tot}} = \sum_{n=1}^{N_g} E_n \tag{45}$$

3. Determine the wavenumber  $\eta^*$  from the random number relations of the selected gas species,  $R_{\eta,g,n^*}$ , rescaled from  $R_{\eta,i}^k$  [26]. A database for each gas species random number versus temperature and wavenumbers built from spectroscopy datasets, such as HITEMP [28], must be available for this scheme. Wavenumbers are determined from the database by using interpolation for  $T_{g,i}$  and using a bi-sectional search for  $\eta^*$  [26].

If the emitting phase is a solid phase, then the steps for the wavenumber selection are as follows,

- 1. Select a random number for each ray in a cell,  $R_{n,i,m}^k$
- 2. For each random number, determine the corresponding wavenumber,  $\eta^*$ , from the random number relations

$$R_{\eta,s,m}^{k} = \frac{\int_{0}^{\eta^{*}} \kappa_{\eta,s,m} I_{b\eta} d\eta'}{\int_{0}^{\infty} \kappa_{\eta,s,m} I_{b\eta} d\eta'}.$$
 (46)

The spectral absorption coefficients  $\kappa_{\eta,s,m}$  are approximated using correlations, which can be found in [17,29]. Using these correlations, we derive in the next sub-sections a method for determining the relation between random numbers vs wavenumber and other physical properties.

**Table 3:** Representative values for complex index of refractions [29].

|                     | m = n - ik       | $C_0$ |
|---------------------|------------------|-------|
| coal                | m = 2.05 - 0.54i | 3.143 |
| char (fixed carbon) | m = 2.20 - 1.12i | 5.023 |
| ash                 | m = 1.50 - 0.02i | 0.189 |

The particle absorption coefficient correlations of Buckius and Hwang [17] define a normalized absorption coefficient

$$\kappa_s^* = \kappa_{\eta,s}/f_A,\tag{47}$$

where  $f_A$  is the total cross-sectional area per unit volume defined as

$$f_A = \int_0^\infty \pi r^2 n(r) \mathrm{d}r,\tag{48}$$

where r is the particle radius and n(r) is the per volume number density. The correlations for the normalized absorption coefficient depend on particle properties combined together as

$$\kappa_{s0}^* = \Im\left[\frac{m^2 - 1}{m^2 + 2}\right] \frac{6\pi\varepsilon_s \eta}{f_A} = C_0 \frac{\varepsilon_s}{f_A} \eta,\tag{49}$$

where m = n - ik is the complex index of refraction, i is the imaginary number,  $\Im()$  denotes the imaginary part, and  $C_0$  is the complex index of refraction coefficient,

$$C_0 = \frac{36\pi nk}{(n^2 - k^2 + 2)^2 + 4n^2k^2},\tag{50}$$

The *n* and *k* coefficients are the real and imaginary components of the complex index of refraction of the solid particle. The complex index of refraction of selected solids are provided in Table 3.

The correlation equation for particle absorption coefficients is [17,29]

$$\kappa_s^* = \left[ \frac{1}{\left(\kappa_{s0}^* (1 + 2.30\kappa_{s0}^{*2})\right)^{1.6}} + \frac{\kappa_0^{*1.76}}{1.66^{1.6}} \right]^{-1/1.6}.$$
 (51)

According to Eqn. (46),  $R_{\eta,s}$  depends on three variables  $\kappa_{s0}^*$ ,  $\eta$ ,  $T_s$ . The following substitutions make subsequent correlations more convenient: letting

$$\xi = \frac{\eta}{T_s},\tag{52}$$

and

$$\gamma = C_0 \frac{\varepsilon_s}{f_A} T_s,\tag{53}$$

then,

$$\kappa_{s0}^* = \gamma \xi, \tag{54}$$

and the random number relation, Eqn. (46), can be reexpressed in terms of the new variables  $\gamma$  and  $\xi$  as

$$R_{\eta,s} = \frac{\int_0^{\xi} \kappa_s^*(\gamma \xi') I_{b\xi}(\xi') \mathrm{d}\xi'}{\int_0^{\infty} \kappa_s^*(\gamma \xi') I_{b\xi}(\xi') \mathrm{d}\xi'},\tag{55}$$

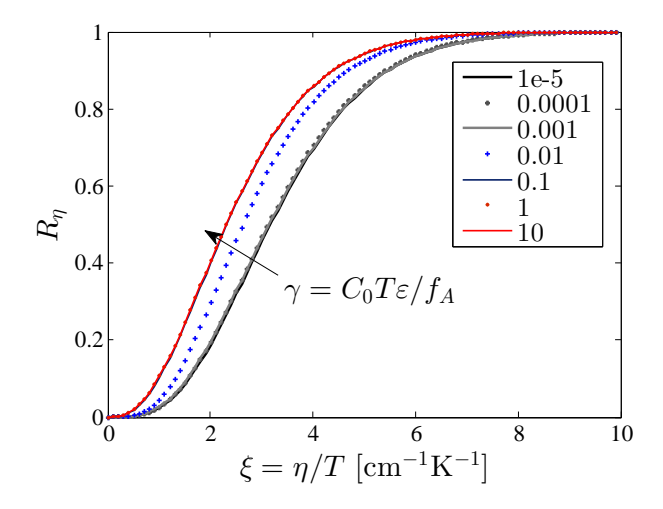


Figure 8: Random number relations and curve-fitting coefficients for particles.

where  $\kappa_s^*$  is now a function of  $\gamma \xi$ , and  $I_{b\xi}$  is a modified Planck function,

$$I_{b\xi} = \frac{I_{b\eta}}{T_s^3} = \frac{C_1 \xi^3}{\pi (\exp C_2 \xi - 1)}.$$

The range of  $\xi$  is  $0 < \xi < \infty$ , since  $0 < \eta < \infty$ ; however, the range of  $\gamma$  is finite.

Focusing on  $\kappa_s^*$ , we may expect three regimes according to particle sizes: small, intermediate, and large particles. In the limiting case where  $\kappa_0^* \ll 1$  (small particles), Eqn. (51) gives

$$\kappa_{\rm s}^* \approx \gamma \xi.$$
(56)

At the other extreme, where  $1 \ll \kappa_0^*$  (large particles), Eqn. (51) may be reduced to

$$\kappa_s^* \approx 1.66(\gamma \xi)^{-1.1}.\tag{57}$$

Since  $\gamma$  can be factored out of the integrations in Eqn. (55) at the limit when particles are either too small or too large, we can expect  $R_{\eta,s}$  to be sensitive to the value of  $\gamma$  only for intermediate particles sizes. This is illustrated with numerical calculations of  $R_{\eta,s}$  shown in Fig. 8. Profiles of  $R_{\eta,s}$  vs.  $\eta$  overlap if  $\gamma$  exceeds lower and upper limiting values.

The following algebraic expression was found to approximate  $R_{\eta,s}$  very well for various values of  $\gamma$ ,

$$R_{\eta,s}(\gamma,\xi) = \frac{1}{2} + \frac{1}{2} \tanh\left(a_1(\gamma)\xi^{0.4} - a_2(\gamma)\right). \tag{58}$$

This expression is readily inverted to obtain  $\eta$  as a function of  $R_{\eta}$  and other properties. The fitting coefficients  $a_1$  and  $a_2$  were determined successively for  $-6 < \lg \gamma < 2$ , where  $\lg$  is the base 10 logarithm, using least-squares minimization. A plot of the values for  $a_1$  and  $a_2$  is shown in Fig. 8. As  $\gamma$  tends to small values of  $\gamma < 10^{-5}$ , coefficients  $a_1$  and  $a_2$  no longer change, as expected. Likewise, as  $\gamma$  tends to large values of  $\gamma > 1$ , the coefficients  $a_1$  and  $a_2$  again remain constant. In order to produce a curve fit with the algebraic expression in Eqn. (58), we use curve-fitting function

| Table 4: Correlation | coefficients fo | or random ni | imber relations  |
|----------------------|-----------------|--------------|------------------|
| Table 4: Correlation | coefficients to | n tanuoni ni | amber refations. |

| ioi fandoni number felations. |          |              |              |              |       |
|-------------------------------|----------|--------------|--------------|--------------|-------|
|                               | $b_{ij}$ | j = 1        | <i>j</i> = 2 | j = 3        |       |
|                               | i = 1    | 2.358        | 3.469        |              |       |
|                               | i = 2    | 2.390        | 3.260        |              |       |
|                               | i = 3    | 3.010        | 2.010        | 2.742        |       |
|                               | $c_{ij}$ | <i>j</i> = 1 | <i>j</i> = 2 | <i>j</i> = 3 | j = 4 |
|                               | i = 1    | 2.358        | 3.469        | 2.443        | 4.114 |
|                               | i = 2    | 2.390        | 3.260        | 2.526        | 4.078 |
|                               | i = 3    | 3.010        | 2.010        | 2.742        | 2.169 |

with two asymptotes corresponding to those of Fig. 8b. The coefficients  $a_1$  and  $a_2$  are, therefore, fitted according to

$$a_1(\gamma) = \frac{b_{11}}{\exp\left[c_{12}(\lg \gamma + c_{11})\right] + 1} + \frac{b_{12}}{\exp\left[-c_{14}(\lg \gamma + c_{13})\right] + 1}$$
(59)

$$a_2(\gamma) = \frac{b_{21}}{\exp\left[c_{22}(\lg \gamma + c_{21})\right] + 1} + \frac{b_{22}}{\exp\left[-c_{24}(\lg \gamma + c_{23})\right] + 1}$$
(60)

where values of the coefficients  $c_{ij}$ , for i = 1, 2, and j = 1, ..., 4, are given in Table 4.

### Planck-mean absorption coefficients for solid phases

The Planck-mean absorption coefficients are directly calculated using the Buckius and Hwang [17] correlations for  $\kappa_s$  given by Eqn. (51),

$$\bar{\kappa}_s^*(\gamma) = \bar{\kappa}_s / f_A = \frac{\pi}{\sigma} \int_0^\infty \kappa_s^*(\gamma \xi) I_{b\xi}(\xi) d\xi. \tag{61}$$

Here we introduced the normalized Planck-mean absorption coefficient  $\bar{\kappa}_s^*$  which depends only on  $\gamma$ . Data obtained from direct numerical calculations of Eqn. (61) for  $-6 < \lg \gamma < 2$  are shown in Fig. 9a as a function of  $\lg \gamma$ . It is more convenient to consider the variation of  $\lg(\bar{\kappa}_s^*/\gamma)$  as a function of  $\lg \gamma$  as shown in Fig. 9b. For the small particle limiting case,  $\lg(\bar{\kappa}_s^*/\gamma)$  approaches a constant value of 2.425. For the large particle limiting case,  $\lg(\bar{\kappa}_s^*/\gamma)$  approaches a linear relation with  $\lg \gamma$  as indicated by the line equation in Fig. 9b. In order to capture the two limiting cases and the intermediate cases, we apply the function with parameters to be obtained through least-squares curve-fitting,

$$\lg\left(\frac{\bar{\kappa}_s^*}{\gamma}\right) = \frac{b_{31}}{\exp\left[c_{32}(\lg\gamma + c_{31})\right] + 1} - \frac{b_{32}\lg\gamma + b_{33}}{\exp\left[-c_{34}(\lg\gamma + c_{33})\right] + 1}$$
(62)

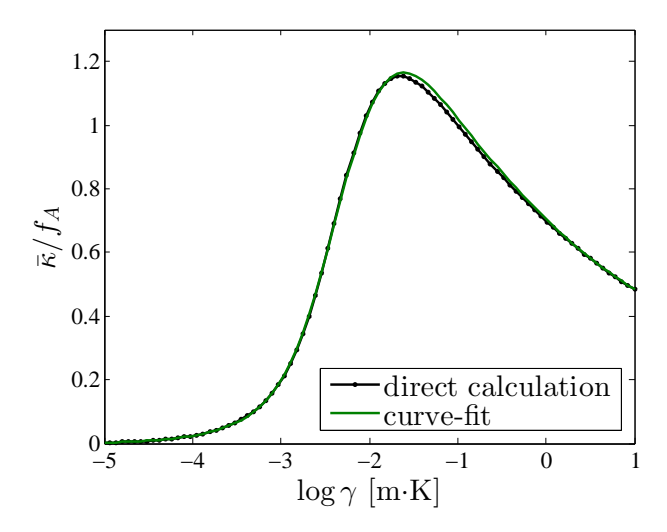
The fitting coefficients,  $c_{3j}$ , with j = 1, ..., 4, are given Table 4.

#### Absorption energy splitting across phases

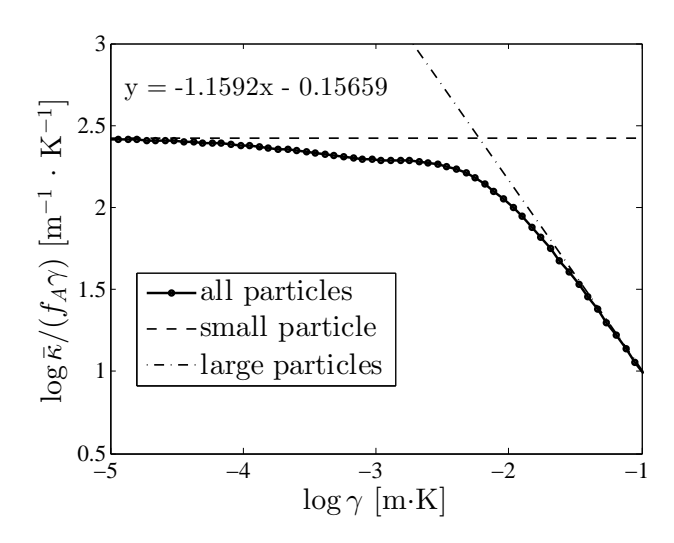
The amount of absorbed energy by cell  $c_j$  from the kth photon bundle emitted from cell  $c_i$  is computed as

$$Q_{\text{abs},ij}^k = Q_{ij}^k \left( 1 - \exp(-\Delta \tau_{\eta,ij}^k) \right). \tag{63}$$

The quantity in parentheses is the absorptivity of cell  $c_j$ , which depends on the local optical distance  $\Delta \tau_{\eta,ij}^k$ . The spectral variable  $\eta$  is based on the random number relations given earlier for a given photon bundle associated with indices (i,k). The optical thickness in cell  $c_i$  for the kth ray



(a) Normalized Planck-mean absorption coefficient



(b) Ratio of normalized Planck-mean absorption coefficient and solids property variable  $\boldsymbol{\gamma}$ 

**Figure 9:** Directly calculated and curve-fitted Planck-mean absorption coefficients for particles as functions of  $\gamma$ .

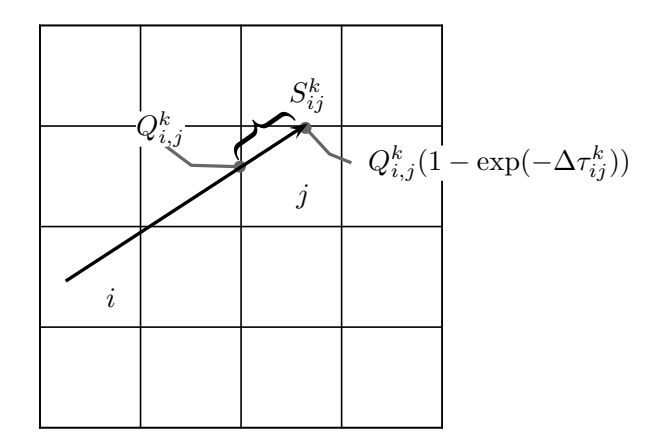


**Figure 10:** Illustration of a single ray emitted from cell  $c_i$  and traversing cell  $c_j$ . The absorbed energy is based on the absorptivity of cell  $c_j$ .

is computed as

$$\Delta \tau_{\eta,ij}^{k} = \kappa_{\eta_{i}^{k},j} S_{ij}^{k} = \left( \kappa_{\eta_{i}^{k},g,j} + \sum_{m=1}^{N_{s}} \kappa_{\eta_{i}^{k},sm,j} \right) S_{ij}^{k}.$$
 (64)

The factor in parentheses of this equation represents the effective absorption coefficient of the cell. The distance traveled by the ray through the cell is represented by  $S_{ij}^k$  as shown in Fig. 10. The gas absorption coefficient is equal to the weighted sum of the gas species absorption coefficients,

$$\kappa_{\eta,g,j} = \left(\sum_{n=1}^{N_g} x_{n,j} \kappa_{\eta,g,n,j}\right) p_{g,j} \varepsilon_{g,j} \tag{65}$$

The solid phase absorption coefficients are computed according to the Buckius and Hwang correlations given by Eqn. (51).

The energy of a photon bundle diminishes as it traverses each cell as it is traced according to

$$Q_{ij}^{k} = Q_{i}^{k} - \sum_{j' \in \mathbb{J}_{(i(-1))}^{k}} Q_{\text{abs},ij'}^{k}, \tag{66}$$

where the set  $\mathbb{J}_{i(j-1)}^k$  denotes all cells crossed by the kth ray emitted from cell  $c_i$  before intersecting cell  $c_j$ .

The formulation for absorption partitioning across gas and solid phases is based on the following criterion: If solids m = 1 and m = 2 are identical (same  $\kappa_{\eta,s,m}$ ), then energy splitting should give identical results if the two solids where instead analyzed as a single solid phase. Therefore, the amount of energy absorbed by the mth solid phase must be proportional its volume fraction, or  $Q_{{\rm abs},sm} \propto \varepsilon_{s,m}$ . The solid phase absorption coefficient  $\kappa_{\eta,s}$  is also proportional the volume fraction as can be seen from Eqn. (47),

$$\kappa_{\eta,s} = f_A \kappa_s^* = \frac{3\varepsilon_s}{4\bar{r}_s} \kappa_s^*, \tag{67}$$

where  $f_A = 3\varepsilon_s/(4\bar{r}_s)$ . Note that the gas phase absorption coefficient is also proportional to its volume fraction (Eqn. (65)). Following the approach in [30], the simplest way to satisfy the above

physical criterion is to assign weights for each phase according to

$$w_{\eta_{i}^{k},(g)\text{or}(s,m),j} = \frac{\kappa_{\eta_{i}^{k},(g)\text{or}(s,m),j}}{\kappa_{\eta_{i}^{k},g,j} + \sum_{m=1}^{N_{s}} \kappa_{\eta_{i}^{k},s,m,j}},$$
(68)

and compute the absorbed energies by the gas and solid phase as

$$Q_{\text{abs},(g)\text{or}(s,m),j} = \sum_{i,k \in \mathbb{I}_j, \mathbb{K}_j} Q_{\text{abs},ij}^k w_{\eta_i^k,(g)\text{or}(s,m),j} .$$

$$(69)$$

The valid i and k indices are such that the kth ray has intersected cell  $c_j$ , denoted by the sets  $\mathbb{I}_j$ , and  $\mathbb{K}_j$ .  $Q_{ij}^k$  is the incoming ray energy as it intersects the cell according to Eqn. (66). Note that the spectral variable  $\eta$  depends on the random number relations of the emitting phase and that the total absorption is summed over randomly selected wavenumbers, thereby accounting for the spectral integration of the radiative transfer.

#### Sample calculations

The LBL-PMC method is demonstrated with a some sample problems in this section. The configuration of each of the example problems are axisymmetric 1- or 2-D. Therefore, the examples given here are based on the procedures for axisymmetric PMC tracing described in [31].

The radiative source  $S_{rad}$  for each energy equation may be calculated as

$$S_{\text{rad},(g)\text{or}(sm),i} = -\nabla \cdot \mathbf{q}_{(g)\text{or}(sm),i}$$

$$= \frac{Q_{\text{abs},(g)\text{or}(sm),i} - Q_{\text{emi},(g)\text{or}(sm),i}}{V_i},$$
(70)

where the phase absorption  $Q_{\text{abs},(g)\text{or}(sm),i}$  is given by Eqn. (69), and the phase emission  $Q_{\text{emi},(g)\text{or}(sm),i}$  is given by Eqn. (33).

First we consider a homogeneous medium with one gas phase and one solid phase, both at 650K. The medium is enclosed by a cylinder with cold, black walls ( $T_w = 0$  and  $\varepsilon_w = 1$ ). The volume fraction of the solid phase is  $\varepsilon_s = 0.01$  and is composed of solid coal particles with an average radius of  $\bar{r}_s = 10 \ \mu \text{m}$ .

The LBL-PMC method is applied to obtain the absorbed energy  $Q_{\rm abs}^{\prime\prime\prime} = Q_{\rm abs}/V$  for each phase, as shown in Fig. 11a. In this case, the absorption of radiation for each phase is comparable to each other. The lower absorption trend at the wall is due to the cylinder wall absorbing emitted radiation. The absorption of the gas is relatively flatter because  $CO_2$  strongly reabsorbs what it emits. The absorption profiles calculated with the LBL-PMC are in close agreement with the *exact* solutions [29], which are also shown.

As another example relevant to fluidized-bed problems, we consider a medium which contains a freeboard and bed section. Using the geometry described in the previous example, the lower half (0 < z < 0.5m) of the cylindrical enclosure consists of the bed section, and the upper half (0.5m< z < 1m) consists of the freeboard section. In the bed section, the volume fraction of gas is  $\varepsilon_g = 0.99$  and the volume fraction of the solid phase is  $\varepsilon_s = 0.01$ . In the freeboard section, the volume fraction of gas is  $\varepsilon_g = 0.999$  and the volume fraction of the solid phase is  $\varepsilon_s = 0.001$ . In both section the gas has 10% CO<sub>2</sub> mole fraction and the average solid particle is  $10^{-5}$ m. The gas and solid temperature in both sections are set to  $T_g = T_s = 650$ K.

Profiles of  $Q_{abs}^{""}$  taken along the centerline of the cylindrical enclosure (r = 0) are shown in Fig. 12. In the bed section, where the volume fraction of the solid phase is greater, most of the radiation is due to the solid phase, while in the freeboard section, the gas phase radiation is dominant. This example problem was also used to validate the spectral PMC energy partitioning by comparing with *exact* solutions [29].

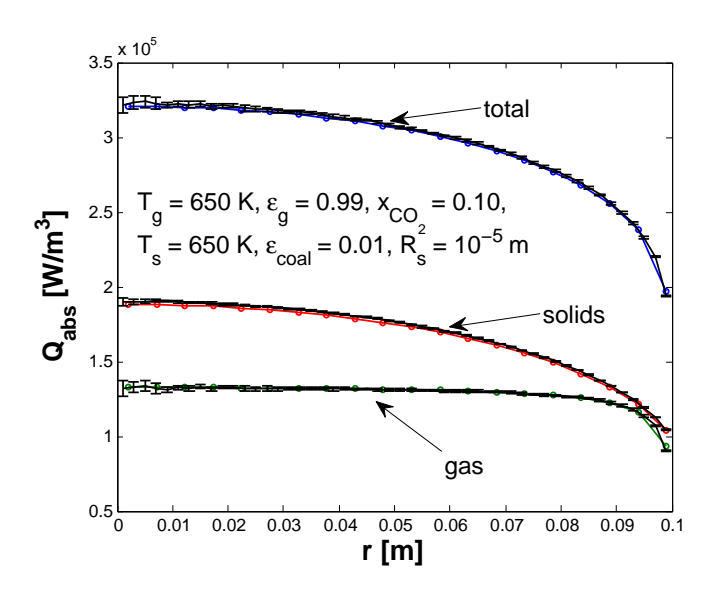


**Figure 11:** Line-by-line PMC and Exact solutions of  $Q_{abs}$  with a uniform property mixture of  $CO_2$  gas and coal solid phase within a cylindrical enclosure.

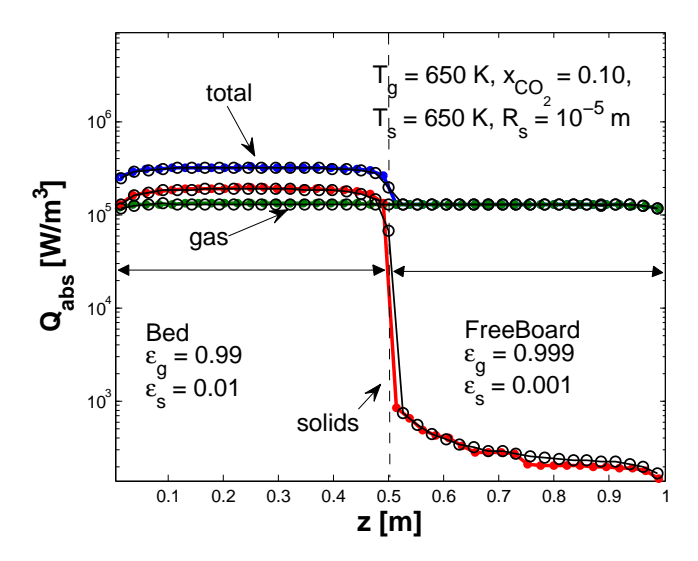


**Figure 12:** Line-by-line PMC and Exact solution of  $Q_{abs}$  for fluidized-bed. Profiles are taken along the centerline axis (r = 0).

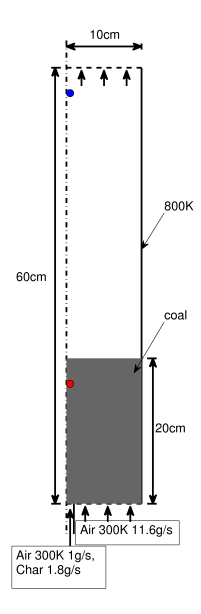


Figure 13: Flow geometry

#### 2.5 Test and Validation Runs

To demonstrate the importance of radiation in fluidized beds and in pulverized coal combustion, as well as the power of the here developed models, a few test cases with radiative feedback will be described.

# Fluidized-bed coal combustor with radiation via regression scheme

A fluidized-bed coal combustion case is utilized to study the radiation in coal combustors. Four gas phase species are considered, namely  $O_2$ , CO,  $CO_2$  and  $N_2$ . Solid particles are modeled by two solid phases: cold-char and hot-char. Each solid phase has two pseudo-species: fixed-carbon and ash. Only the carbon content in the hot-char phase is reactive to gas species following the reactions

$$C + \frac{1}{2}O_2 \longrightarrow CO \tag{71}$$

$$C + CO_2 \longrightarrow 2CO$$
 (72)

One gas species reaction is also considered:

$$CO + \frac{1}{2}O_2 \longrightarrow CO_2 \tag{73}$$

Finally a pseudo reaction converts solid particles from cold-char to hot-char to model the char heating up process

$$Cold-char \longrightarrow Hot-char \tag{74}$$

The fluidized-bed coal combustor is chosen to be cylindrical (Fig. 13), with a radius of 10cm and a height of 60cm. The bottom 10cm of the combustor are filled with uniform char particles of 1mm diameter. The char particles have a complex refractive index  $\mathbf{m} = 2.2 - 1.12i$  [24]. Two coaxial jets are utilized to fluidize the bed particles. The central jet has a radius of 1cm and supplies a cold gas-particle mixture (300K) at mass flow rates of 1g/s for air and 1.8g/s for char. The annulus jet has an outer radius of 10cm and supplies cold air (300K) at a mass flow rate of 11.6g/s. The particles

in the bed remain approximately at 1000K. The wall temperature is 800K. A two-dimensional uniform cylindrical mesh is used, which has 20 cells in the radial direction and 60 cells in the axial direction.

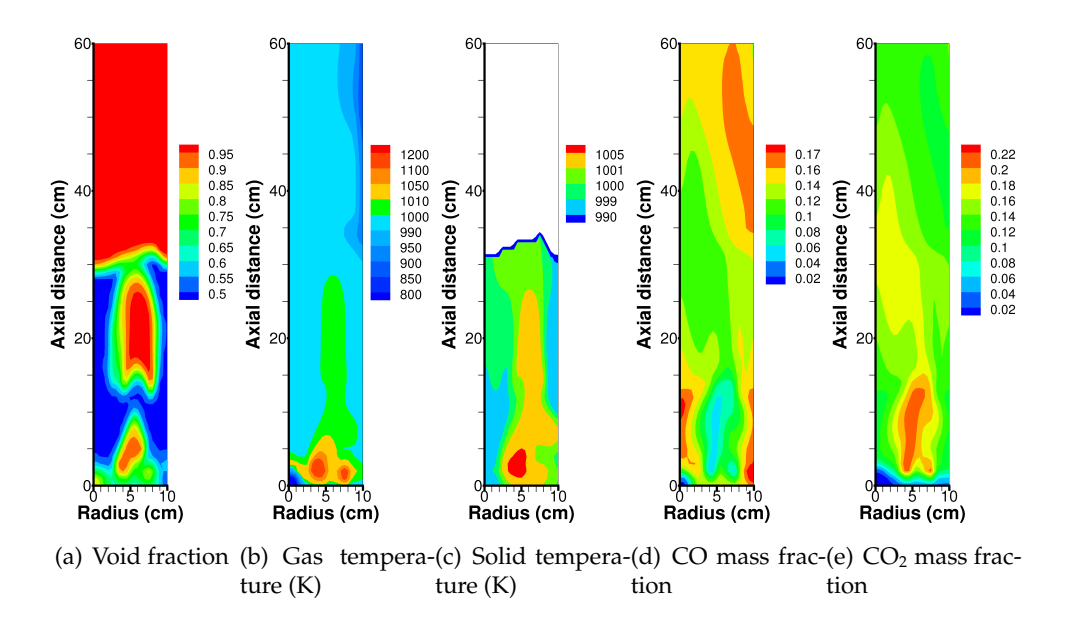


Figure 14: Instantaneous flow fields

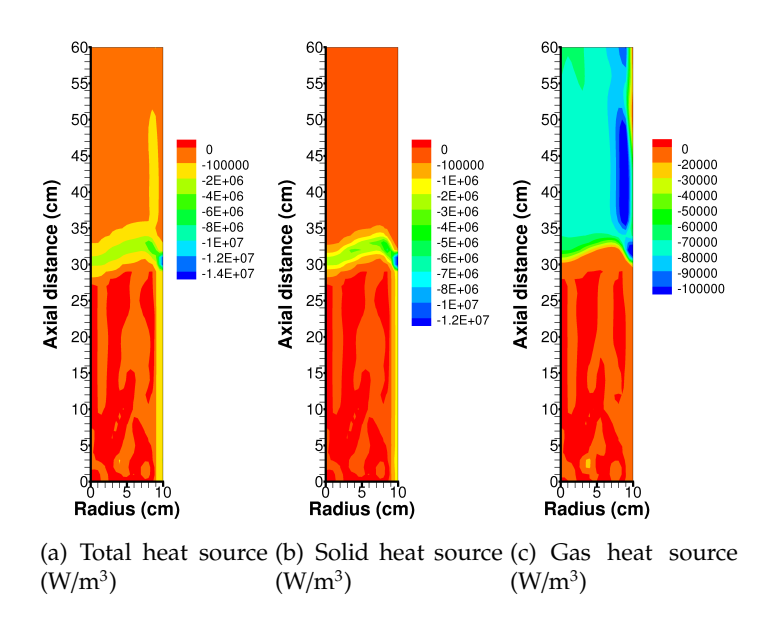


Figure 15: Instantaneous radiative heat sources

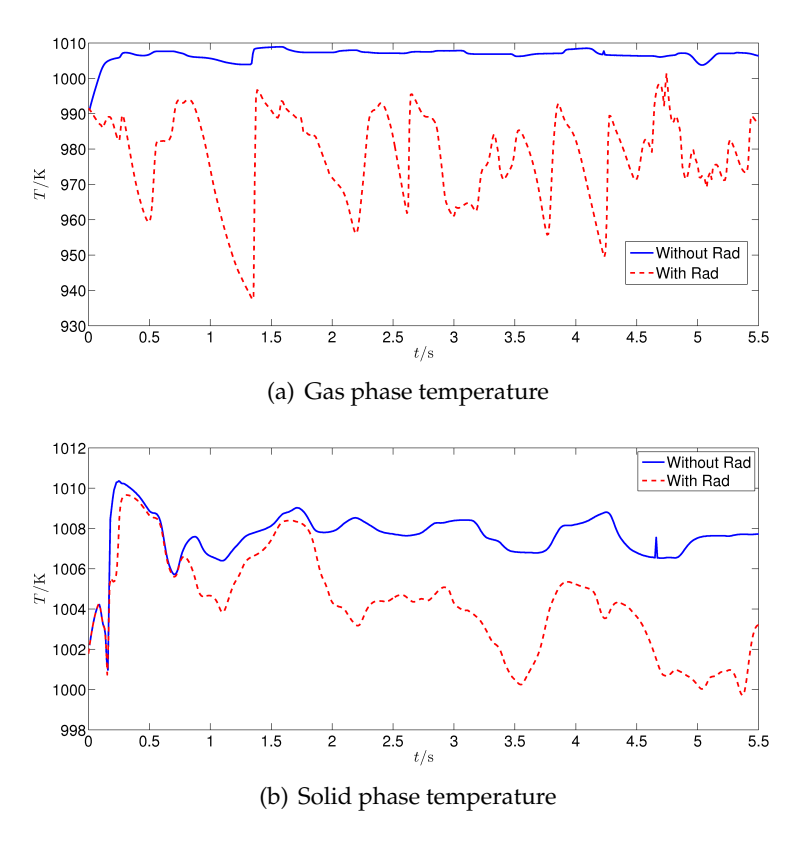
Instantaneous snapshots of the flow fields without radiation are given in Fig. 14. The void fraction is shown in Fig. 14(a), the high void fractions in the bed suggesting rising bubbles. Temperatures of the gas and solid phases are shown in Figs. 14(b) and 14(c), respectively. Because of small solid volume fraction in the freeboard, the temperature of the solid phase is not defined and thereby truncated for solid volume fractions lower than 0.01, resulting in a blank freeboard in

Fig. 14(c). Due to the high temperature of the solid phase in the bed, reactions start immediately when air is in contact with solid particles at the bottom of the bed. The chemical reactions at the bottom of the bed generate higher gas and solid temperatures. Near the gas bubbles the solid volume fraction is smaller (higher void fraction at the bottom Fig. 14(a)), which results a lower heat capacity of the solid phase and the solid temperature peaks near r = 5cm at the bottom of the bed. However, due to the large solid specific heats (as compared to the gas), temperature variations of the solid phases are small (within 10K) in the rest of the bed. The gas phase temperature (Fig. 14(b)) achieves equilibrium with the solid temperature after passing through the solid bed. Above the solid bed, the gas is cooled in the boundary layer along the wall. CO is formed immediately when air is on contact with solid particles at the bottom of the bed (Fig. 14(d)), followed right away by  $CO_2$  formation (Fig. 14(e)). Near a gas bubble, the abundant  $O_2$  further reacts with CO and results in peak  $CO_2$  mass fraction (Fig. 14(e)) and a corresponding valley in CO mass fraction.

The total as well as phase-separated radiative heat sources are shown in Fig. 15. Due to the large absorption coefficients of solid particles, the radiative heat sources of the solid phases are only observed within a layer along the surface to the wall or to the freeboard (Fig. 15(b)). The layer with significant radiative heat sources is a few centimeters thick. The exact thickness depends on the volume fraction of the solids near the surface. For example, near the wall the solid volume fraction is larger than near the top surface adjacent to the freeboard, resulting in a thinner radiation layer, which is expected because of the resulting larger extinction coefficients. Within the surface layer with considerable radiation, the solid heat source is an order of magnitude higher than that of the gas. Inside the bed, small radiative heat sources are observed for both gas and solid phases, since both gas and solid temperatures are nearly uniform and the total absorption coefficient is large. In particular, both gas and solid radiative heat sources are near zero at the bottom of the bed, where major heat releasing reactions take place with the formation of CO and CO<sub>2</sub>. As a result, adding radiative heat transfer does not quench the reactions. The gas radiation peaks between 1 and 3cm away from the wall in the freeboard (Fig. 15(c)). Closer to the wall (within 1cm), the gas temperature drops in the boundary layer causing less radiative emission. Further away from the wall, outside the thermal boundary layer, the incident radiation becomes larger causing more radiative absorption. The competition between these two phenomena results in a maximum negative heat source in the gas phase at the edge of thermal boundary layer.

The temporal evolutions of gas and solid temperature with and without radiation are compared in Fig. 16, both starting with identical flow fields. The gas temperature temporal sequence shown in Fig. 16(a) is sampled at 0.25cm radius and 56.5cm height in the free board, as marked with a blue dot in Fig. 13. Since the position is outside the thermal boundary layer, there is no convective heat loss. Therefore, without radiation the gas temperature quickly reaches a higher value and has small temporal fluctuations. With radiation, the gas temperature is lower by approximately 30K and fluctuates more due to concentration fluctuations of CO and CO<sub>2</sub>, which are strong radiators. The solid phase temperature shown in Fig. 16(b) is sampled at 0.25cm radius and 16.5cm height inside the bed, as also marked with a red dot in Fig. 13. The solid phase temperature drifts at a rate of slightly more than 1K/s (due to slow decrease of coal/increase of ash in the bed) and fluctuates more when radiation is considered. However, the net radiative heat source at this location is negligible as shown in Fig. 15, suggesting that the solid temperature drops and fluctuates because of blending cooler particles from the surface after radiative heat loss.

Evolving flow fields, such as volume fractions, temperatures and species mass fractions, were solved both with and without radiation. Time averaged fields are obtained by averaging over 5 s corresponding to 10 times the residence time of the gas flow. Time averaged void fraction, and CO and CO<sub>2</sub> mass fractions without radiation are shown in Fig. 17. These fields are barely changed when radiation is considered.



**Figure 16:** Time evolution of temperature of gas and solid phases between with and without radiation starting from the same field. The gas temperature is sampled at 0.25cm radius and 56.5cm height in the free board (marked with a blue dot in Fig. 13). The solid phase temperature is sampled at 0.25cm radius and 16.5cm height inside the bed (marked with a red dot in Fig. 13).

The time averaged temperatures of gas and solid phases with and without radiation are compared in Fig. 18. To make the impact of radiation more visible, the temperatures without radiation are accompanied by the temperature differences after radiation is considered. Without radiation the temperature of the gas phase (Fig. 18(a)) is relatively constant in the freeboard outside the thermal boundary layer. With radiation, the temperature continuously drops when gas flows through the freeboard due to radiative emission by CO and  $CO_2$  (Fig. 18(b)). Outside the boundary layer the only heat loss is due to radiation. Within 2cm from the wall, the temperature decrease in the gas phase due to radiation is less in the thermal boundary layer, because of strong convective effects. In the bed, the temperature difference of the gas phase between with and without radiation is the same as that in the solid phase because the gas-solid mixture is in thermal equilibrium. For the time-averaged temperature of the solid phase without radiation (Fig. 18(c)) and the temperature difference with radiation (Fig. 18(d)), results are truncated for the region where mean solid volume fraction is less than 0.05 (i.e. mean void fraction larger than 0.95 in Fig. 17(a)) because of lack of statistical meaning. With radiation being considered, the solid temperature is slightly reduced (less than 15K), but only near the surface to the freeboard.

The time-averaged radiative heat sources of gas and solid phases are shown in Fig. 19. For the gas phase (Fig. 19(a)), most radiative heat loss occurs in the freeboard, consistent with the temperature decline in the freeboard shown in Fig. 18(b). For the same reason mentioned in the discussion of instantaneous gas radiative heat source, the time-averaged radiative heat source is most negative at about 2cm away from the wall. This also corresponds to the greatest temperature

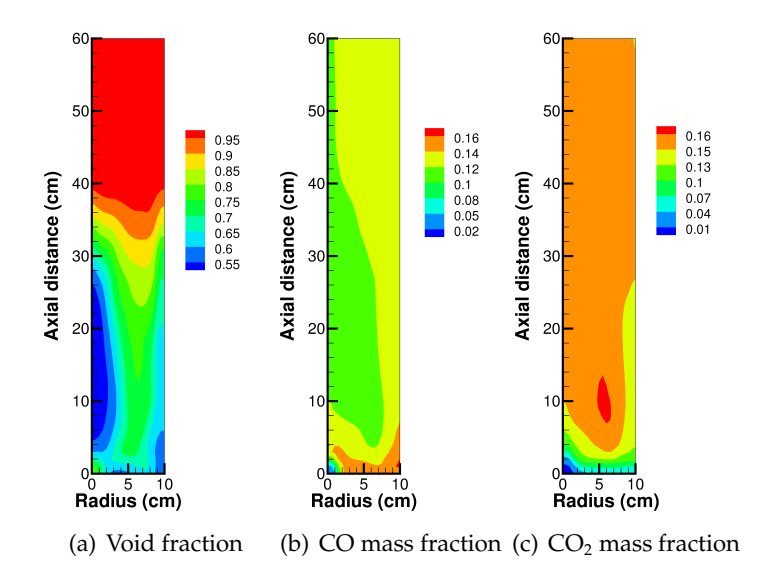


Figure 17: Time averaged flow fields

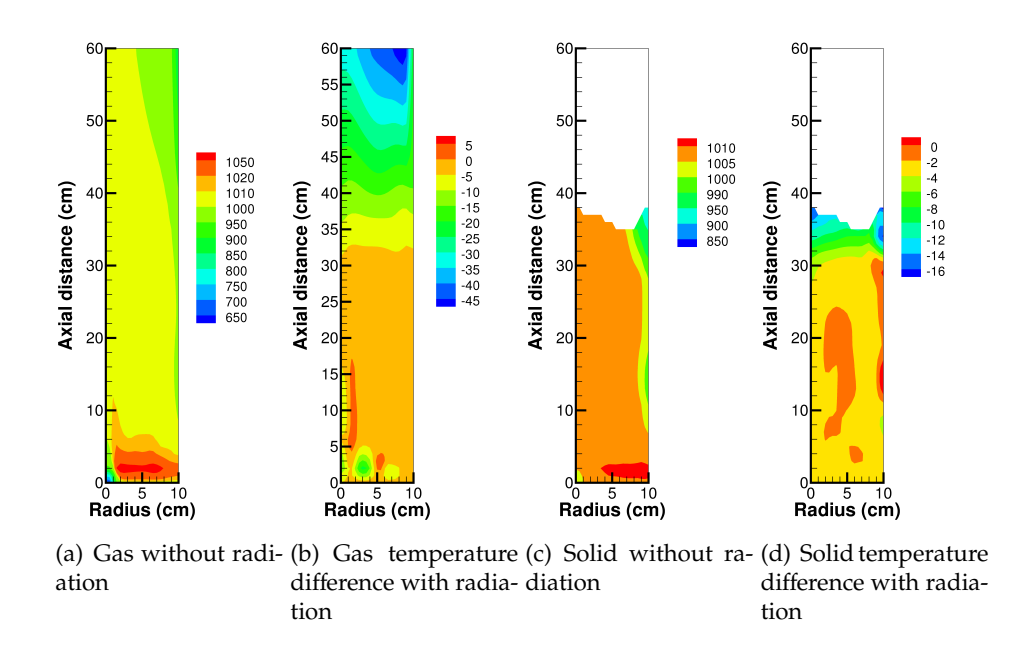


Figure 18: Time-averaged temperature field

decline in the gas phase at this radial location as shown in Fig. 18(b). Inside the bed, the radiative heat source of the gas is zero, corresponding to the zero temperature difference in Fig. 18(b). In particular, the magnitude of the radiative heat source is small at the bottom of the bed where heat releasing reactions take place, i.e., radiation does not quench the reactions. The solid phase heat source is shown in Fig. 19(b), truncated above the freeboard boundary as in Fig. 18(c). The radiative heat source of the solid phase is only significant near the top of the bed at the surface to the freeboard or near the wall. The heat source at the surface to the freeboard causes the temperature decline shown in Fig. 18(d). Near the wall, convection dominates the heat transfer in the solid phase, thereby no temperature difference is observed (Fig. 18(d)).

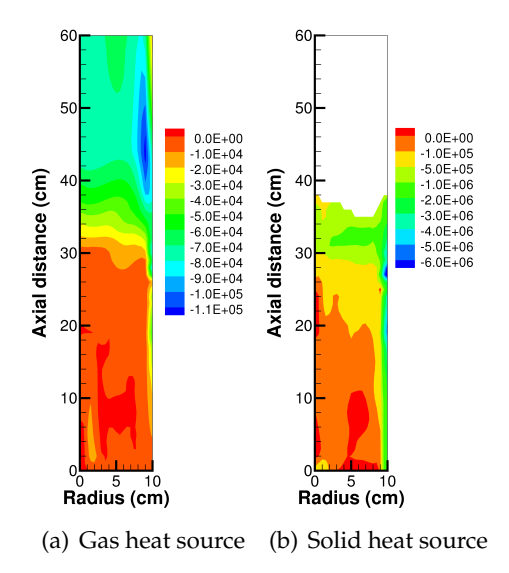


Figure 19: Time-averaged heat sources

A cylindrical fluidized-bed coal combustor was chosen to study radiation feedback in packed gas-particle flows using the multi-phase PMC module. The combustor has a radius of 10cm and a height of 60cm. The bottom 10cm of the combustor are filled with uniform char particles of 1mm diameter. Two coaxial jets are utilized to fluidize the bed particles. The central jet has a radius of 1cm and supplies a cold gas-particle mixture (300K) at mass flow rates of 1g/s for air and 1.8g/s for char. The annulus jet has an outer radius of 10cm and supplies cold air (300K) at a mass flow rate of 11.6g/s. The particles in the bed remain approximately 1000K. The wall temperature is 800K. A two-dimensional uniform cylindrical mesh is used, which has 20 cells in the radial direction and 60 cells in the axial direction. The bed of such a combustor is optically very opaque, making it almost impossible to analyze with a PMC scheme; the problem, therefore, is meant to test the limits of the here developed module. Figure 20 shows the 2D axisymmetric MFIX grid system employed, and Fig. 21 shows the temporal temperature variations at the two locations indicated in Fig. 20, the first being in the bed, the other in the freeboard. Temperatures shown are temporal values averaged over the cells indicated for a 10s duration. It is seen that temperatures with and without radiation are fairly similar, due to the fact that both bed and freeboard are optically extremely thick, making radiation a diffusion phenomenon.

#### Validation against an experimental pulverized flame

The target flame for validation purposes is a pulverized coal jet flame piloted by a methane flame [32]. Coal particles are entrained by air through a central jet. The central jet diameter is 6mm. Methane is injected through an annular slit between co-axial central and annular jets.

The thermophysical properties of the coal in the simulation are based on reported values with some simplifications, and are listed in Table 5. Moisture contained in the coal is instead added to the carrier gas, because drying is a fast process under high heating rates and completes before coal particles are ignited. The sulfur and nitrogen components are combined with oxygen from ultimate analysis, as this study focuses on combustion and heat transfer modeling instead of pollution prediction.

The kinematic properties include a coal feed rate of  $1.49 \times 10^{-4}$  kg/s, central jet air flow rate of  $1.8 \times 10^{-4}$  m<sup>3</sup>/s, and methane flow rate of  $2.33 \times 10^{-5}$  m<sup>3</sup>/s. The corresponding Reynolds number was

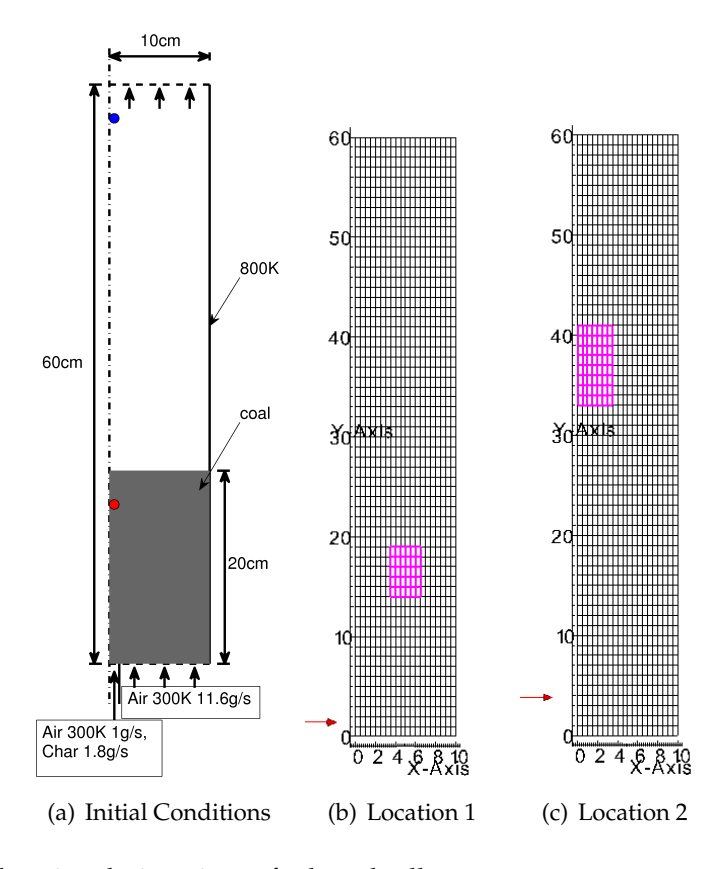


Figure 20: Mesh and location designations of selected cells.

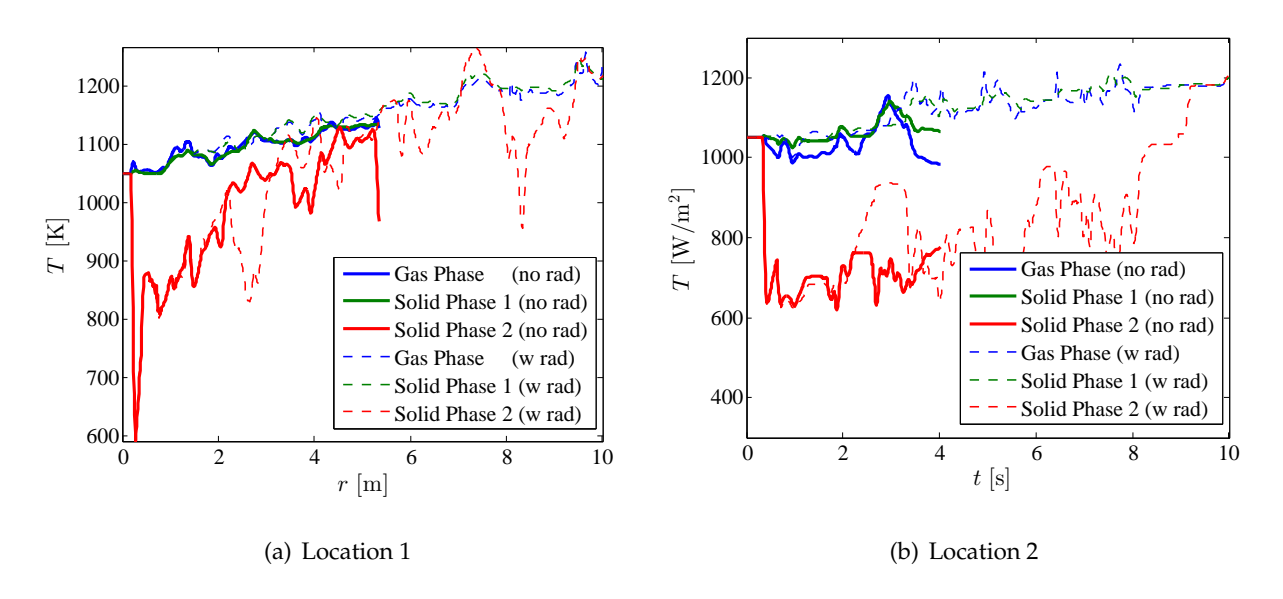


Figure 21: Volume averaged temperature time series at locations 1 and 2.

| parameter                 | value     |  |
|---------------------------|-----------|--|
| low heating value         | 28.1MJ/kg |  |
| proximate analysis (wt %) |           |  |
| fixed carbon              | 57.9%     |  |
| ash                       | 15.2%     |  |
| volatile matter           | 26.9%     |  |
| ultimate analysis (wt %)  |           |  |
| carbon                    | 71.9%     |  |
| hydrogen                  | 4.4%      |  |
| oxygen                    | 8.5%      |  |
| oxygen                    | 8.5%      |  |

**Table 5:** Thermophysical properties.

reported as 2544. Laser Doppler Velocimetry (LDV) was used for particle velocity measurements. Particle temperature was determined from a two color radiation pyrometer based on wavelengths of 0.9 and 1.0  $\mu$ m.

Three solid phases are considered for particle size distributions in the Eulerian-Eulerian framework. The underlying particle size distribution is assumed to be a truncated Rosin-Rammler distribution, with a minimum particle diameter of 5  $\mu$ m, a maximum particle diameter of 61  $\mu$ m, a mean diameter of 25  $\mu$ m and a spreading parameter of 4.0. The mean particle size of 25  $\mu$ m was reported in the original experimental paper. This distribution is binned into three phases with equal probability. The nominal particle sizes ( $d_{32}$ ) of the three phases are 16.6, 24.8 and 35.9  $\mu$ m, respectively. Their volume fractions relative to the total solid phases are 0.063, 0.237 and 0.70, respectively.

The computational domain is two dimensional axisymmetric 3cm in radius from the jet axis and 25cm in height from the jet exit. Radial and axial directions are uniformly discretized into 120 and 100 cells respectively. A parabolic velocity profile is used for the central jet inlet velocity, and a free slip wall boundary condition is used at the far field.

Additional physical models were added to address important processes not directly supported by MFIX: Turbulent mixing of gas species and enthalpy are modeled by turbulent diffusivities that are related to turbulent viscosity through unity turbulent Schmidt number and Prandtl number, respectively. Turbulent dispersion of pulverized particles with a size less than  $50\mu$ m, which are assumed to follow turbulent eddy motions, is modeled through a turbulent diffusivity. The solid turbulent diffusivity is identical to diffusivity of the gas species. The gaseous turbulent combustion model invoked here is the Eddy Dissipation Concept (EDC) model [33]. The EDC model assumes that the local mass fraction of each species decays toward its chemical equilibrium composition. The decay rate is related to turbulent flow fields. The coal devolatilization model employed is Kobayashi's two rates model [34]. This model defines two competing devolatilization rates of Arrhenius form. The total rate of devolatilization is the sum of the two, i.e.,

$$\frac{dm_{\text{vol}}}{dt} = -\left[\alpha_1 B_1 \exp(-E_1/RT_p) + \alpha_2 B_2 \exp(-E_2/RT_p)\right] m_{\text{vol}}$$
(75)

The model parameters are identical to the original reference:

$$\alpha_1 = 0.3$$
,  $B_1 = 2.0 \times 10^5 \text{s}^{-1}$ ,  $E_1 = 1.05 \times 10^5 \text{J/mol}$   
 $\alpha_2 = 1.0$ ,  $B_2 = 1.3 \times 10^7 \text{s}^{-1}$ ,  $E_2 = 1.67 \times 10^5 \text{J/mol}$ 

In Fig. 22 the temperatures of gas and solid phases without radiation are compared. The peak gas temperature reaches in excess of 2200K, close to the  $\mathrm{CH}_4$  adiabatic flame temperature in air.

Two flame fronts are formed. One is between the methane pilot and the central air–coal jet, the other one is between the methane pilot and ambient air.

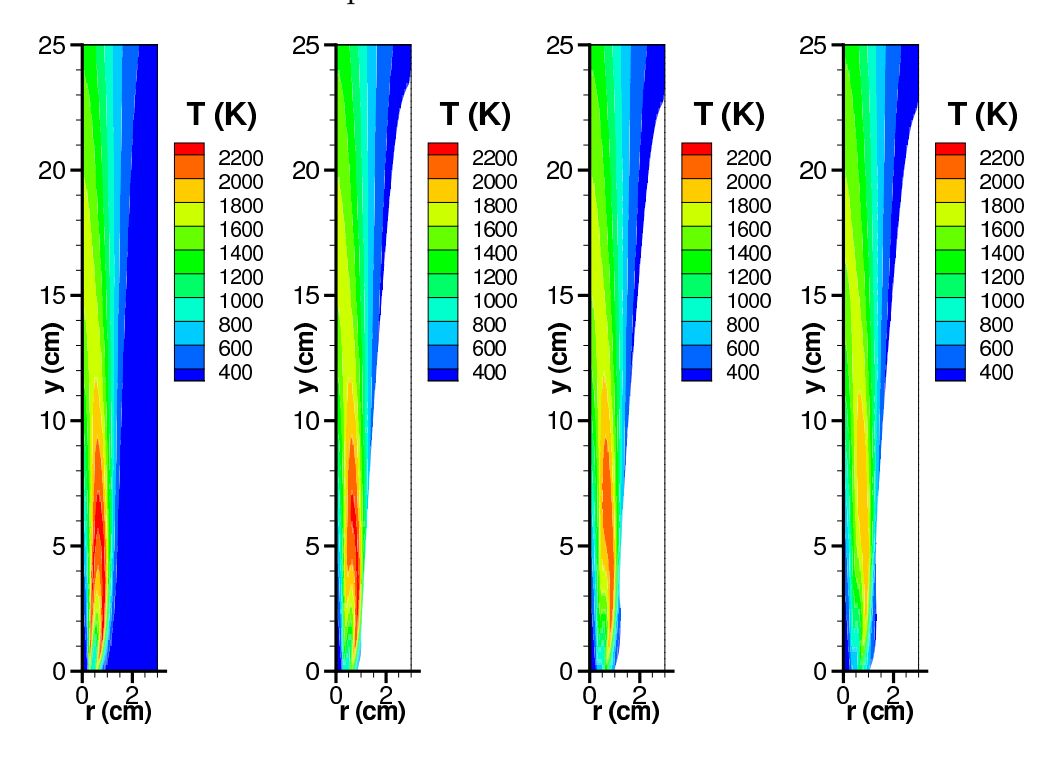


**Figure 22:** Temperatures of separate phases without radiation. From left to right: gas, solid phase 1, solid phase 2 and solid phase 3. White space indicates areas with negligible particle contents.

The solid phase temperature profiles (Fig. 22) are left blank in regions with low volume fractions, because Eulerian phase properties are not properly defined. The solid phases have lower temperature than the gas, in general, because of particle thermal response delay. Smaller particles with shorter response time follow gas phase temperatures more closely. The solid temperatures approach thermal equilibrium with the gas phase in the downstream (i.e., y > 15cm). Upstream solid phases follow gas temperature near the outer front (r > 5mm) of CH<sub>4</sub> flame more closely than near the inner flame front, because smaller solid phase velocity at the outer front leads to longer residence time.

Results with radiation feedback are compared in Figs. 23 and 24 for temperatures, temperature differences between the with- and without-radiation cases, and radiative heat sources, respectively.

The temperatures of gas and solid phases are similar to those without radiation since they are controlled by chemical reactions (Fig. 23). The influence of radiation on temperature is further illustrated by the temperature difference fields shown in Fig. 24. With the consideration of radiation, the gas phase temperature drops by over 180K at a location of 20cm above the nozzle. Solid phases that emit stronger experience stronger cooling effects on flame temperature. Diffused combustion products (gases and particles) away from the flame (r > 1.5cm and y > 15cm) at lower temperature absorb radiation from the flame and acquire slight higher temperature.

Radiative heat sources are shown in Fig. 25 and turn out to be mostly negative (i.e., emission exceeds absorption). The magnitudes of the radiative heat source align with the temperature of that phase. Both observations confirm that emission dominates radiation in this flame. The cooling effects from these radiative heat sources are not instant and depend on residence time. This is also observed in Fig. 24, e.g., the highest temperature drop is downstream from the peak flame

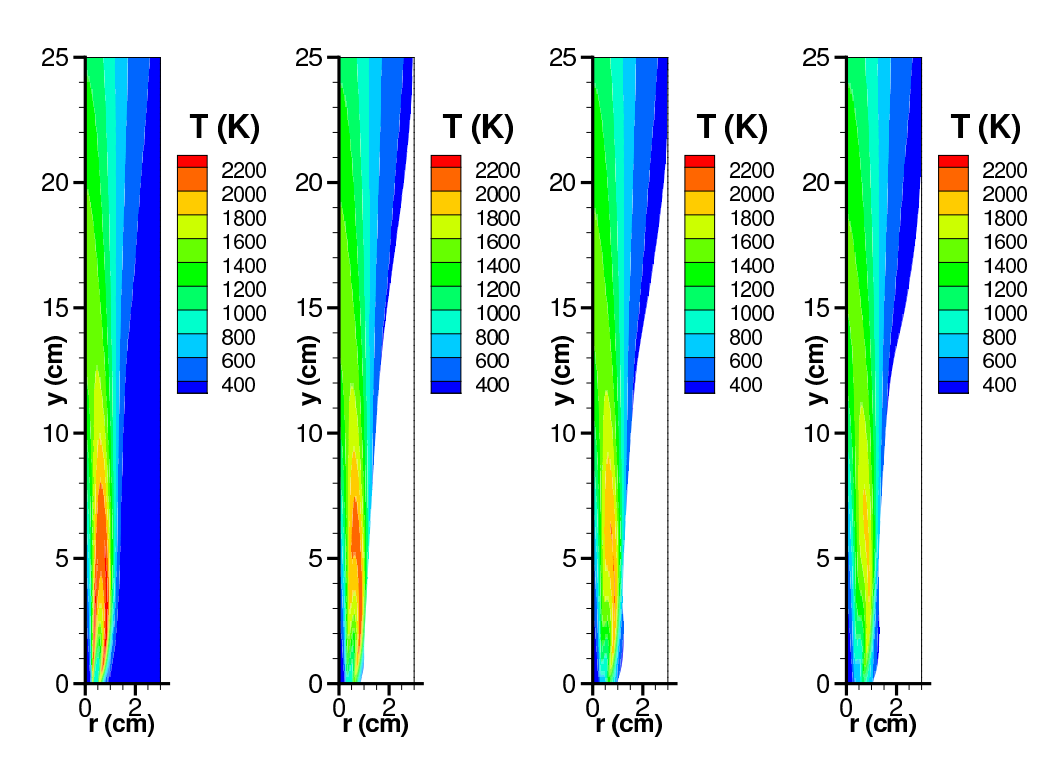


**Figure 23:** Temperature of each phase with radiation feedback. From left to right: gas, solid phase 1, solid phase 2 and solid phase 3.

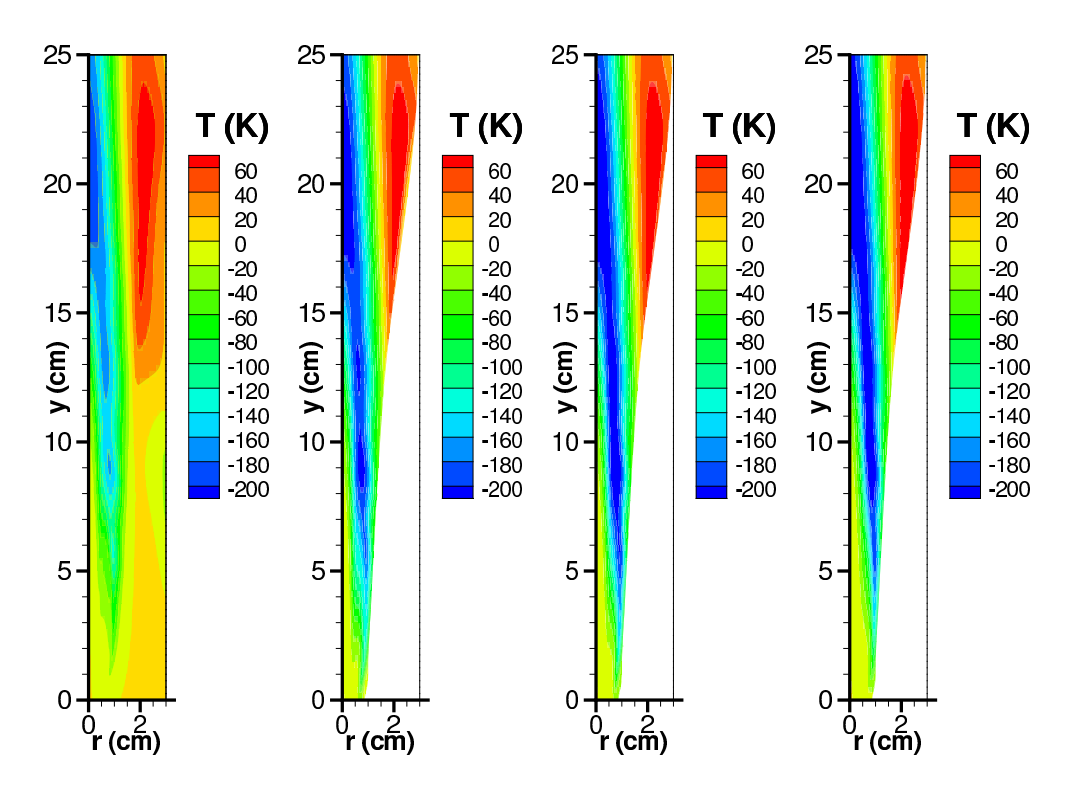


**Figure 24:** Temperature differences of each phase between with and without radiation. From left to right: gas, solid phase 1, solid phase 2 and solid phase 3.

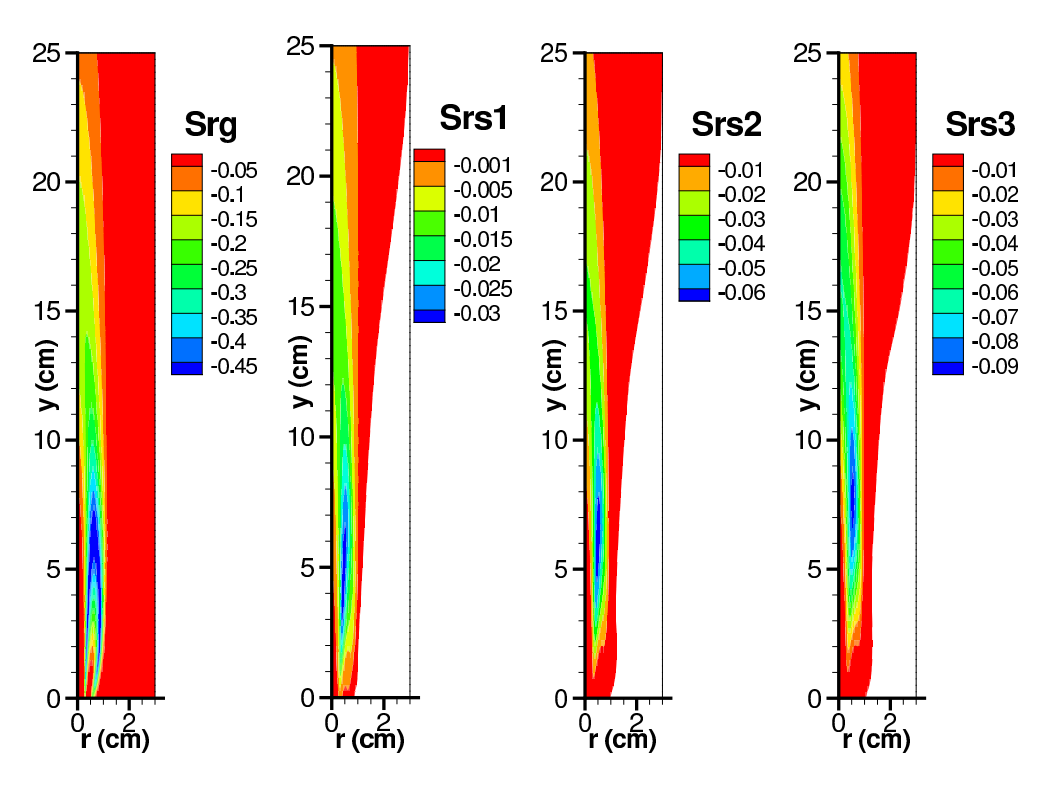


**Figure 25:** Radiative heat sources of each phase. From left to right: gas, solid phase 1, solid phase 2 and solid phase 3. Unit is cal/(cm<sup>3</sup>s).

#### temperature location.

Although radiation is included through the radiative heat source in the energy conservation equations only, it also produces indirect effects on other flow variables, such as species concentrations through the temperature-dependent reaction rates. In Fig. 26 the  $\rm CO_2$  and  $\rm H_2O$  mass fractions are compared for the with- and without-radiation cases. With radiation the  $\rm CO_2$  mass fraction is reduced downstream (i.e.,  $y > 15 \rm cm$ ). In this region radiative heat loss causes gas and particle temperatures in the flame to drop by over 100K. This temperature drop significantly reduces char reaction rates and leads to a lower levels of  $\rm CO_2$ . The mass fraction of  $\rm H_2O$  is also affected, but to a lesser extent. In the current model  $\rm H_2O$  forms from hydrogen elements in coal particles through devolatilization and volatile combustion. Both processes complete in the upstream (i.e.,  $y < 15 \rm cm$ ) where coal particles are heated and yield the same  $\rm H_2O$  generation. Therefore, the flame shows less variations of  $\rm H_2O$  mass fraction.

In the original flame measurements, the particle temperature is inferred from a two-color pyrometer operating at 0.9 and  $1.0\mu m$ . Such a pyrometer measures line-of-sight flame radiation at two wavelengths. The ratio of radiation intensity at two wavelengths is compared to that from blackbody emission. This method is mostly used for surface temperature measurement, as surface emissivity is close at two close wavelengths. However, its use in flame measurements requires additional caution since the pyrometer readout does not reflect the particle temperature at any location, nor the average temperature along the line-of-sight because of the nonlinear dependence of radiation emission on temperature. In order to make a direct comparison, flame emission is calculated here using flow field variables and integrated along a line-of-sight using particle properties at these two wavelengths. The ratio of integrated intensities is compared against a blackbody intensity ratio. This synthesizes the pyrometer readout from the predicted flow fields.

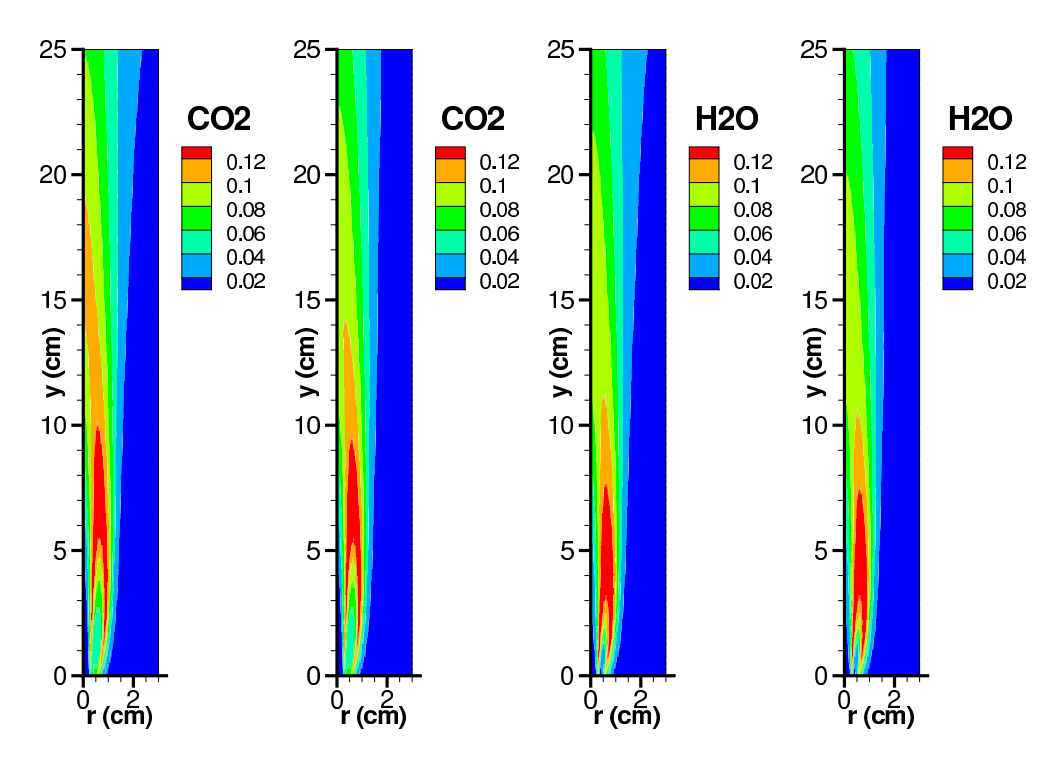


**Figure 26:** Comparison of gas species mass fraction between with and without radiation feedbacks. From left to right:  $CO_2$  without radiation,  $CO_2$  with radiation,  $H_2O$  without radiation and  $H_2O$  with radiation.

The temperature predictions are compared with experiments in Fig. 27. The temperature profiles along the centerline are drawn in red. The radial peak temperature at fixed height are shown as blue lines. The black lines show numerical prediction of the pyrometer readout. It is clear that pyrometer readout differ from both centerline and and peak profiles, although the predicted readout captures the overall cooling trends.

#### 3 Summary

Several radiation solvers for fluidized-bed and pulverized coal combustion have been developed, and have been implemented in two open source CFD codes, viz. OpenFOAM and MFIX. A database for radiative properties of common coals has been collected, to be used with, both, conventional and stochastic radiative solvers. A  $P_1$  RTE solver paired with a regression-based spectral scheme was developed and imbedded into both OpenFOAM and MFIX, followed by thorough testing. In parallel, a stochastic photon Monte Carlo solver was also developed, which allows for line-by-line accurate spectral resolution. This module was also imbedded into both OpenFOAM and MFIX. For validation and testing several fluidized-bed and pulverized coal combustion cases have been studied. The resulting radiation modules, several error fixes and needed extensions to MFIX, as well as the necessary manuals have been communicated to NETL personnel.

# **References Cited**

1. W. Jones and M. C. Paul, Combination of DOM with LES in a gas turbine combustor, *Int. J. of Engineering Science* 43 (5–6) (2005), 379–397.

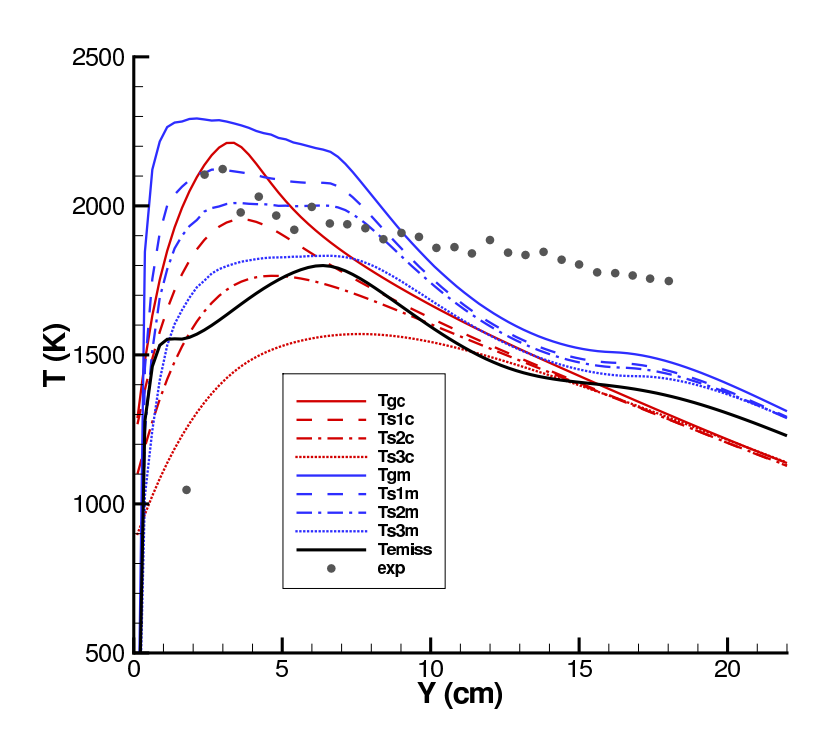


Figure 27: Emission temperature differences of each phase between with and without radiation.

- 2. P. Schmitt, T. Poinsot, B. Schuermans and K. P. Geigle, Large-eddy simulation and experimental study of heat transfer, nitric oxide emissions and combustion instability in a swirled turbulent high-pressure burner, *J. Fluid Mech.* 570 (2007), 17–46.
- 3. R. W. Bilger, Turbulent diffusion flames, Ann. Rev. Fluid Mech. 21 (1989), 101–135.
- 4. R. W. Bilger, Future Progress in Turbulent Combustion Research, *Progr. Energy Combust. Sci.* 26 (2000), 367–380.
- 5. A. A. Townsend, The Effects of Radiative Transfer on Turbulent Flow of a Stratified Fluid, *J. Fluid Mech.* 4 (1958), 361–375.
- 6. G. M. Shved and R. A. Akmayev, Influence of Radiative Heat Transfer on Turbulence in Planetary Atmospheres, *Atmos. and Oceanic Phys.* 34 (1977), 1286–1401.
- 7. T.-H. Song and R. Viskanta, Interaction of Radiation with Turbulence: Application to a Combustion System, *J. Thermoph. Heat Transfer* 1(1) (1987), 56–62.
- 8. A. Soufiani, P. Mignon and J. Taine, Radiation–Turbulence Interaction in Channel Flows of Infrared Active Gases, In *Proceedings of the Ninth International Heat Transfer Conference*, Vol. 6, pp. 403–408, Hemisphere, Washington, D.C. (1990).
- 9. R. J. Hall and A. Vranos, Efficient Calculations of Gas Radiation From Turbulent Flames, *Int. J. Heat Mass Transfer* 37 (1994), 2745.
- 10. L. Wang, D. C. Haworth, S. R. Turns and M. F. Modest, Interactions among soot, thermal radiation, and NOx emissions in oxygen-enriched turbulent nonpremixed flames: a CFD modeling study, *Comb. Flame* 141(1-2) (2005), 170–179.

- 11. L. Wang, M. F. Modest, D. C. Haworth and S. R. Turns, Modeling Nongray Soot and Gas-Phase Radiation in Luminous Turbulent Nonpremixed Jet Flames, *Comb. Th. Mod.* 9(3) (2005), 479–498.
- 12. Y. Hua, G. Flamant, J. Lu and D. Gauthier, 3D modelling of radiative heat transfer in circulating fluidized bed combustors: influence of the particulate composition, *Int. J. Heat Mass Transfer* 48 (2005), 1145–1154.
- 13. D. E. Alagoz, G. Kulah and N. Selçuk, A comprehensive fluidized bed combustion model coupled with a radiation model, *Comb. Sci. T.* 180 (2008), 910–926.
- 14. M. F. Modest, Radiative Heat Transfer (2nd Edn), Academic Press, New York (2003).
- 15. A. Wang and M. F. Modest, High-accuracy, compact database of narrow-band *k*-distributions for water vapor and carbon dioxide, *J. Quant. Spectrosc. Radiat. Transfer* 93 (2005), 245–261.
- 16. M. F. Modest and R. J. Riazzi, Assembly of Full-Spectrum *k*-Distributions from a Narrow-Band Database; Effects of Mixing Gases, Gases and Nongray Absorbing Particles, and Mixtures with Nongray Scatterers in Nongray Enclosures, *J. Quant. Spectrosc. Radiat. Transfer* 90(2) (2005), 169–189.
- 17. R. O. Buckius and D. C. Hwang, Radiation Properties for Polydispersions: Application to Coal, *J. Heat Transfer* 102 (1980), 99–103.
- 18. K. H. Im and R. K. Ahluwalia, Radiation Properties Of Coal Combustion Products, *Int. J. Heat Mass Transfer* 36(2) (1993), 293–302.
- 19. J. Taine, A Line-by-Line Calculation of Low-Resolution Radiative Properties of CO<sub>2</sub>–CO–Transparent Nonisothermal Gases Mixtures up to 3000 K, J. Quant. Spectrosc. Radiat. Transfer 30(4) (1983), 371–379.
- 20. H. Zhang and M. F. Modest, A Multi-Scale Full-Spectrum Correlated-*k* Distribution For Radiative Heat Transfer in Inhomogeneous Gas Mixtures, *J. Quant. Spectrosc. Radiat. Transfer* 73(2–5) (2002), 349–360.
- 21. L. Wang and M. F. Modest, Narrow-Band Based Multi-Scale Full-Spectrum *k*-Distribution Method for Radiative Transfer in Inhomogeneous Gas Mixtures, *J. Heat Transfer* 127 (2005), 740–748.
- 22. M. F. Modest, Narrow-band and full-spectrum *k*-distributions for radiative heat transfer—correlated-*k* vs. scaling approximation, *J. Quant. Spectrosc. Radiat. Transfer* 76(1) (2003), 69–83.
- 23. G. Pal and M. F. Modest, A narrow-band based multi-scale multi-group full-spectrum *k*-distribution method for radiative transfer in nonhomogeneous gas–soot mixture, *J. Heat Transfer* 132 (2010), 023307–1–023307–9.
- 24. M. P. Mengüç and R. Viskanta, On the Radiative Properties of Polydispersions: A Simplified Approach, *Comb. Sci. T.* 44 (1985), 143–159.
- 25. A. Wang and M. F. Modest, Spectral Monte Carlo Models for Nongray Radiation Analyses in Inhomogeneous Participating Media, *Int. J. Heat Mass Transfer* 50 (2007), 3877–3889.
- 26. T. Ren and M. F. Modest, Hybrid wavenumber selection scheme for line-by-line photon Monte Carlo simulations in high-temperature gases, *J. Heat Transfer* 135(8) (2013), 084501.
- 27. R. S. Mehta, D. C. Haworth and M. F. Modest, Composition PDF/photon Monte Carlo Modeling of Moderately Sooting Turbulent Jet Flames, *Comb. Flame* 157 (2010), 982–994.

- 28. L. S. Rothman, I. E. Gordon, R. J. Barber, H. Dothe, R. R. Gamache, A. Goldman, V. I. Perevalov, S. A. Tashkun and J. Tennyson, HITEMP, the high-temperature molecular spectroscopic database, *J. Quant. Spectrosc. Radiat. Transfer* 111(15) (2010), 2139–2150.
- 29. M. F. Modest, Radiative Heat Transfer (3rd Edn), Academic Press, New York (2013).
- 30. P. von Zedtwitz, W. Lipiński and A. Steinfeld, Numerical and experimental study of gasparticle radiative heat exchange in a fluidized-bed reactor for steam-gasification of coal, *Chem. Eng. Sci.* 62 (2007), 599–607.
- 31. A. M. Feldick and M. F. Modest, An Improved Wavelength Selection Scheme for Monte Carlo Solvers Applied to Hypersonic Plasmas, *J. Quant. Spectrosc. Radiat. Transfer* 112 (2011), 1394–1401.
- 32. S. M. Hwang, R. Kurose, F. Akamatsu, H. Tsuji, H. Makino and M. Katsuki, Application of optical diagnostics techniques to a laboratory-scale turbulent pulverized coal flame, *Energy & Fuels* 19(2) (2005), 382–392.
- 33. B. Magnussen, The Eddy Dissipation Concept: A Bridge between Science and Technology, In *ECCOMAS Thematic Conference on Computational Combustion, Lisbon, Portugal*, (2005).
- 34. H. Kobayashi, J. Howard and A. Sarofim, Coal devolatilization at high temperatures, *Symposium* (*International*) on *Combustion* 16(1) (1977), 411 425.